

**Understanding the Role of Soluble Inorganic Ions on the Cytocompatibility and  
Biodegradation of Bioceramic Biodegradable Coatings and Resorbable Calcium Phosphate  
Cement**

by

**John Michael Ohodnicki**

B.S in Bioengineering, University of Pittsburgh, 2013

Submitted to the Graduate Faculty of the  
Swanson School of Engineering in partial fulfillment  
of the requirements for the degree of  
Master of Science in Bioengineering

University of Pittsburgh

2019

UNIVERSITY OF PITTSBURGH

SWANSON SCHOOL OF ENGINEERING

This thesis was presented

by

**John Michael Ohodnicki**

It was defended on

November 13, 2019

and approved by

Harvey Borovetz, PhD, Distinguished Professor of Bioengineering, Robert L. Hardesty Professor of Surgery, Professor of Chemical and Petroleum Engineering

Howard Kuhn, PhD, Professor, Department of Industrial Engineering

Abhijit Roy, PhD, Assistant Professor, Department of Bioengineering

Thesis Advisor: Prashant N. Kumta, PhD, Edward R. Weidlein Chair Professor, Departments of Bioengineering, Chemical and Petroleum Engineering, Mechanical Engineering and Materials Science

Copyright © by John Michael Ohodnicki

2019

# **Understanding the Role of Soluble Inorganic Ions on the Cytocompatibility and Biodegradation of Bioceramic Biodegradable Coatings and Resorbable Calcium Phosphate Cement**

John Michael Ohodnicki, MS

University of Pittsburgh, 2019

Biodegradable scaffolds have been researched extensively over the years due to their promise in regenerative medicine and tissue engineering. Several biodegradable biopolymers, bioceramics, and bioresorbable metals have been the focus of research. The degradation rates of these biodegradable scaffolds have a strong influence on the structural integrity, cytocompatibility, and overall biocompatibility of the scaffold. During degradation, it is imperative that the scaffold not elicit any local or systemic toxicity caused by the biodegradation products, in particular, the dissolved ions released from the scaffold. Thus, recent work has focused on implementing methods to alter the degradation rates of various biodegradable scaffolds demonstrating their safety and efficacy while also evaluating their overall effect on in-vitro cytocompatibility. Current research is targeted at understanding the degradation of ion substituted resorbable calcium phosphate (CaP) bone cement and inorganic ion containing coatings on bioresorbable magnesium alloys.

The objective of this research is to understand the influence of soluble ions on 1) the corrosion resistance and degradation of a micro-arc oxidized (MAO) ceramic coating on lithium-aluminum-and zinc (LAZ) and lithium-zinc (LZ) Mg based alloys and 2) the cementing reaction and dissolution of a strontium (Sr) substituted dicalcium phosphate dihydrate (DCPD) and amorphous calcium phosphate (ACP) based bone cement. The degradation and dissolution rates of the two systems serves to understand the effect of soluble ions on the in-vitro cytocompatibility

of the scaffolds. Results indicate that the increased corrosion resistance and associated decrease in release of Mg, Li, and Zn ions of MAO coated LAZ631 enables direct cell seeding and proliferation of MC3T3 preosteoblasts. Additionally, 10 and 15 mol% substitution of  $\text{Sr}^{2+}$  in the DCPD-ACP based cements allows the formation of a highly porous cement comprising Sr containing hydroxyapatite (HAp), the mineralized matrix of natural bone. The Sr substituted HAp cement formed following the final setting reaction facilitates a constant  $\text{Sr}^{2+}$  release over a 21-day period promoting increased cytocompatibility of MC3T3 preosteoblasts determined by Live/dead staining and MTT assay conducted at days 1 and 4 of culture in the growth media. Results show the potential of these bioresorbable scaffolds for future investigations in tissue engineering and regenerative medicine.

## Table of Contents

Preface.....	xiv
1.0 Introduction.....	1
1.1 Bone injury and repair.....	1
1.2 Permanent scaffold materials .....	2
1.2.1 Scaffold Requirements.....	2
1.2.2 Types of Materials.....	2
1.2.3 Drawbacks .....	4
1.3 Biodegradable Bone Tissue Engineering Scaffolds .....	4
1.3.1 Osteoblasts .....	5
1.3.2 Osteoclasts.....	6
1.3.3 Osteocytes.....	6
1.3.4 Biodegradable scaffold material types .....	7
1.3.4.1 Synthetic polymers.....	7
1.3.4.2 Natural Polymers .....	7
1.3.4.3 Metals.....	8
1.3.4.4 Calcium phosphate ceramics and cements .....	8
1.3.5 Advantages of Biodegradable scaffolds.....	9
1.4 Biodegradable hydroxyapatite forming calcium phosphate bone cements.....	10
1.4.1 Calcium phosphate (CaP) phases .....	10
1.4.2 Cement setting reaction .....	10
1.4.3 Limitations of hydroxyapatite forming calcium phosphate cements .....	12

1.4.4 Role of strontium ions .....	12
1.5 Biodegradable magnesium alloys .....	14
1.5.1 Corrosion mechanism .....	14
1.5.2 Micro-arc oxidation coating .....	15
2.0 Thesis goals .....	18
2.1 Specific aim 1 .....	18
2.2 Specific Aim 2 .....	19
3.0 Biodegradable Bioceramic Micro-Arc Oxidation Coating on Lithium-Aluminum-Zinc (LAZ) and Lithium-Zinc (LZ) Magnesium Alloys.....	20
3.1 Introduction .....	20
3.2 Materials and methods.....	21
3.2.1 Substrate preparation .....	21
3.2.2 Micro-arc oxidation coating .....	22
3.2.3 Electrochemical corrosion testing.....	22
3.2.4 In-vitro static immersion degradation testing .....	23
3.2.5 Coating characterization .....	24
3.2.6 Ion release measurements.....	24
3.2.7 Mouse preosteoblast cell (MC3T3-E1) culture.....	25
3.2.8 Live/dead staining .....	25
3.2.9 Direct MTT assay .....	26
3.3 Results.....	26
3.3.1 Materials characterization of MAO coated LAZ and LZ alloys .....	26
3.3.2 In-vitro degradation of MAO coated LAZ and LZ alloys.....	29

3.3.3 In-vitro cytocompatibility of MAO coated LAZ and LZ alloys.....	34
3.4 Discussion .....	37
3.5 Conclusions .....	43
<b>4.0 Resorbable Strontium Substituted Amorphous Calcium Phosphate and Dicalcium Phosphate Dihydrate Based Hydroxyapatite Forming Bone Cement .....</b>	<b>45</b>
4.1 Introduction .....	45
4.2 Materials and Methods .....	47
4.2.1 ACP precipitation .....	47
4.2.2 DCPD and strontium substituted DCPD precipitation .....	47
4.2.3 Powder characterization.....	48
4.2.4 Cement characterization .....	49
4.2.5 Mouse preosteoblast MC3T3-E1 cell culture .....	50
4.2.6 Live/dead staining .....	50
4.2.7 Direct MTT assay .....	51
4.2.8 In-vitro dissolution test .....	51
4.2.9 Statistical Analysis .....	52
4.3 Results.....	52
4.3.1 Powder characterization.....	52
4.3.2 Cement Characterization .....	55
4.3.2.1 Setting time.....	55
4.3.2.2 Phase Composition.....	56
4.3.2.3 Wet compressive strength and % porosity.....	57
4.3.2.4 Cement specific surface area .....	60



4.3.3 In-vitro dissolution and cytocompatibility tests .....	61
4.4 Discussion .....	65
4.5 Conclusions .....	69
5.0 Summary and Future Work .....	70
Bibliography .....	73

## **List of Tables**

<b>Table 1.1 Types of commonly used materials for the fabrication of permanent implants. ...</b>	<b>3</b>
<b>Table 1.2 Typical mechanical properties of materials used to fabricate bone implants .....</b>	<b>3</b>
<b>Table 1.3 Types and properties of commonly used calcium phosphate phases [16]......</b>	<b>10</b>
<b>Table 1.4 The elemental composition of enamel, dentin, and bone [19]. .....</b>	<b>13</b>
<b>Table 1.5 Advantages and disadvantages of various surface treatment methods used to reduce corrosion of Mg alloys. ....</b>	<b>16</b>
<b>Table 3.1 Components of Hank's Balanced Salt Solution.....</b>	<b>23</b>
<b>Table 3.2 Calculated corrosion potential, current density, and corrosion rate from PDP measurements of a) uncoated alloys and b)coated alloys .....</b>	<b>32</b>
<b>Table 4.1 The amount (mol) of the Ca and Sr containing precursors. ....</b>	<b>48</b>
<b>Table 4.2 Powder to liquid ratio used for each cement composition.....</b>	<b>49</b>

## List of Figures

<b>Figure 1.1 Cementing reactions of typical calcium phosphate phases [18].</b>	<b>12</b>
<b>Figure 1.2 Schematic diagram and associated reactions during the corrosion of Mg alloys in simulated body fluid (SBF) [22].</b>	<b>15</b>
<b>Figure 1.3 Schematic diagram of the surface and cross section of micro-arc oxidation coatings [26].</b>	<b>17</b>
<b>Figure 1.4 Corrosion rate of bare and MAO coated AZ91D in a 3% NaCl solution at 37°C [23].</b>	<b>17</b>
<b>Figure 3.1 SEM microstructure and EDX elemental composition of MAO coatings on a) LAZ631, b) LAZ931, c) LZ61, d) LZ91</b>	<b>28</b>
<b>Figure 3.2 XRD diffraction pattern of bare and MAO coated substrates a) LAZ631, b) LZ61, c) LAZ931, and d) LZ91</b>	<b>29</b>
<b>Figure 3.3 Potentiodynamic polarization data collected from coated and uncoated a) LAZ631 and LAZ931 and b) LZ61 and LZ91 within Hank's balanced salt solutions maintained at 37°C. N=4.</b>	<b>30</b>
<b>Figure 3.4 a) Mg, b) Li, c) Al ions released and d) solution pH measurements during static immersion testing in Hank's balanced salt solution maintained at 37°C. N=3, significance determined by <math>p &lt; 0.05</math>.</b>	<b>33</b>
<b>Figure 3.5 Microstructure and elemental composition of MAO coatings on a) LAZ631, b) LAZ931, c) LZ61, and d) LZ91 after 5 weeks immersed in Hank's balanced salt solution maintained at 37°C.</b>	<b>34</b>

<b>Figure 3.6 Live/dead staining of MC3T3-E1 cells after 1 day culutre in growth media on MAO coated a) LAZ631, b) LAZ931, c) LZ61, d) LZ91, and e) tissue culture plastic ( + control).....</b>	<b>35</b>
<b>Figure 3.7 Live/dead staining of MC3T3-E1 cells after 4 days of culture in growth media on a) tissue culture plastic ( + control), b) MAO coated LAZ631, and c) SEM image of fixed cells on the surface of MAO coated LAZ631 after 4 days of culture in growth media. ....</b>	<b>36</b>
<b>Figure 3.8 MTT cell viability of MC3T3-E1 cells in growth media cultured directly on MAO coated LAZ631. N=4, significance determined to be <math>p &lt; 0.05</math>.....</b>	<b>37</b>
<b>Figure 4.1 X-ray diffraction pattern of synthesized precursor powders. * denotes DCPD characteristic peaks (JCPDS 09-0077).....</b>	<b>54</b>
<b>Figure 4.2 SEM images of synthesized a) 0SrDCPD, b) 15SrDCPD, c-d) ACP.....</b>	<b>54</b>
<b>Figure 4.3The average setting times of the cements prepared with a 75:25 ACP:DCPD ratio by weight at a) room temperature and b) 37°C. N=3. ....</b>	<b>55</b>
<b>Figure 4.4 X-ray diffraction spectra of prepared undoped and doped cements after final setting. * denotes DCPD characteristic peaks (JCPDS 09-0077). ^ designates HAp characteristic peaks (JCPDS 09-0432).....</b>	<b>56</b>
<b>Figure 4.5 X-ray diffraction spectra of cements after 14 days immersion in PBS. * denotes DCPD characteristic peaks (JCPDS 09-0077) . ^ designates HA characteristic peaks (JCPDS 09-0432). ....</b>	<b>57</b>
<b>Figure 4.6 Wet compressive strength (N=6) and b) % porosity of cement scaffolds after final setting and immersion in PBS (N=3). Significance was determined by <math>p &lt; 0.05</math>.....</b>	<b>58</b>

<b>Figure 4.7 SEM images of the fracture surface of a) 0SrHA, b) 15SrHA after final setting and c) 0SrHA, d)15SrHA after 14 days immersion in PBS. Arrows indicate pores formed during cement mixing.....</b>	<b>60</b>
<b>Figure 4.8 . SS<sub>ABET</sub> measurements of cement scaffolds after final setting and 14 days of immersion in PBS. N=3 .....</b>	<b>61</b>
<b>Figure 4.9 The concentrations of a) Ca<sup>2+</sup>, b) PO<sub>4</sub><sup>3-</sup>, c) Sr<sup>2+</sup> as measured by ICP and d) pH of cements immersed in cell growth media maintained at 37°C.....</b>	<b>63</b>
<b>Figure 4.10 Live/Dead staining of MC3T3-E1 cells cultured in growth media on a) 0SrHA, b) 5SrHA, c) 10SrHA, d) 15SrHA after 1 day and e) 0SrHA, f)5SrHA, g) 10SrHA, and h) 15SrHA after 4 days. ....</b>	<b>64</b>
<b>Figure 4.11 MTT cell viability of MC3T3-E1 cells in growth media cultured directly on cement samples. N=3.....</b>	<b>64</b>

## **Preface**

First and foremost, I would like to thank my parents, Paul and Marie Ohodnicki. Without their constant love, support, and guidance I would not be the person I am today. Please know that your Yunko appreciates all that you two have done and that none of it goes unnoticed.

I would like to thank my advisor Dr. Prashant N. Kumta. Through his constant support over the past years I have learned a tremendous amount of invaluable knowledge. I am truly grateful for everything you have done for me. I would also like to thank Dr. Abhijit Roy for the countless years of support, coffee breaks, and guidance.

I would also like to thank the funding from the National Science Foundation, Engineering Research Center – Revolutionizing Metallic Biomaterials, Grant# EEC-0812348.

## **1.0 Introduction**

### **1.1 Bone injury and repair**

Bone loss as a result of disease and trauma affects millions globally every year. It is expected that by the year 2020 there will be an estimated 6.6 million orthopedic surgeries performed annually. Due to the estimated number of annual surgeries, the orthopedic market is expected to grow to \$66.2 billion at a Compounded Average Growth Rate (CAGR) of 3.8% [1]. Orthopedic surgeries are needed to treat bone injury or loss arising from numerous different related traumatic conditions or congenital injuries. Some examples include joint repair and replacement, fracture repair, bone reconstruction, spinal surgery, as well as due to fatal diseases such as cancer.

The current gold standard of treatment of care for bone defects is the use of autografts. This process involves using a patient's own bone harvested from a non-injured site to aid in the repair of their injury. Unfortunately, this treatment option does not come without drawbacks. Donor site morbidity, increased patient recovery time, increased risk of infections and surgical time as well as associated complications, blood loss, and limitations of the quantity of available materials are some of these associated drawbacks related to autografts [2]. An alternative method used to repair injured or lost bone tissue is allografting. Allografts are obtained from either a donor or most commonly a cadaver. In addition to the above mentioned drawbacks of autografts, the use of allografts increases the risk for disease transmission, complications due to tissue rejection as well as the quality of the material varies highly due to the age and health of the donor [2].

Finally, a third method used for treating bone injury and bone loss is the use and implantation of permanent or non-degradable synthetic scaffolds. The types of materials used as

synthetic permanent implants, requirements, and corresponding drawbacks of the permanent synthetic scaffolds will be discussed in section 1.2 below.

## **1.2 Permanent scaffold materials**

### **1.2.1 Scaffold Requirements**

Despite the type of material used to fabricate the scaffold, there are certain characteristics that the scaffold should exhibit. Firstly, the scaffold needs to be biocompatible within the human body as to not elicit any host rejection or immune response after implantation. The scaffold must also be wear resistant in order to maintain structural stability and integrity during the implant's lifetime without resulting in the formation of metallic debris leading to metallosis. Additionally, the scaffold must be corrosion resistant to avoid the leaching of potentially toxic materials into the body causing either local or systemic toxicity. Lastly, the scaffold must possess adequate mechanical properties that are dictated by the location and function of the bone that is to be repaired. Mismatch of mechanical properties between the scaffold and the surrounding bone largely by the high modulus of the implant compared to the normal bone can lead to the weakening of the surrounding bone due to stress shielding [3].

### **1.2.2 Types of Materials**

The types of materials used to fabricate permanent bone scaffolds consist of polymers, metals, and ceramics. **Table 1.1** reveals materials of each type that are commonly used to make



permanent scaffolds. The type of material chosen depends on the function of the required implant as well as the mechanical properties that the implant will encounter. Metals such as titanium, stainless steel, and cobalt-chromium alloys are commonly used for load bearing applications. However, polymers due to their low compressive/tensile modulus and ceramics due to their brittle nature are commonly used in non-load bearing applications. The typical range of properties for metals, ceramics, polymers compared to compact bone is described in Table 1.2.

**Table 1.1 Types of commonly used materials for the fabrication of permanent implants.**

Type of Implant	Materials Used
Metal	titanium alloys, stainless steel, gold alloys, cobalt-chromium alloy
Polymer	polymethyl methacrylate, polyethylene, polypropylene, polyetheretherketone
Ceramic	alumina, zirconia, porcelain

**Table 1.2 Typical mechanical properties of materials used to fabricate bone implants**

Properties	Natural bone	Ti alloy	CPC/BVFs	Polymer
Density (g/cm <sup>3</sup> )	1.8–2.1	4.4–4.5	3.14	1.3
Elastic modulus (GPa)	3–20	110–117	35–120	0.2–7
Compressive yield strength (MPa)	130–180	758–1117	20–900	N/A
Tensile yield strength (MPa)	104–120	700–900	3–300	1–27
Fracture toughness(MPam <sup>1/2</sup> )	3–6	55–115	0.7	N/A

### **1.2.3 Drawbacks**

Though the types of permanent bone implant scaffolds discussed above are frequently used to repair bone defects, permanent implants do not come without drawbacks. The major drawback of permanent implants is the potential need for secondary surgeries after initial implantation due to implant failure or host rejection occurring after several months or years following implantation [3, 4]. If a secondary surgery is needed to repair or remove the implant additional problems can arise for the patient such as increased cost, additional recovery time and discomfort, and potentially causing higher risk of infection. In recent years, extensive research has been conducted to develop biodegradable scaffolds that will remove the need for secondary surgeries.

## **1.3 Biodegradable Bone Tissue Engineering Scaffolds**

In an ideal situation, biodegradable bone scaffolds should be capable of inducing and supporting bone regeneration while maintaining sufficient mechanical properties throughout the regeneration process. After initial implantation, the scaffold provides 100% of the mechanical stability to the defect site. As the new tissue is formed, the mechanical requirements are shifted from the implant to the newly formed bone tissue. Therefore, it is imperative that the scaffold degrades at a rate which is similar to the regeneration rate of the newly formed bone tissue. In addition, neither the graft material nor its degradation products should elicit any undesired toxicity or immune response to the surrounding cells and tissues.

After implantation, the implant comes into contact with a multitude of cells, metal ions dissolved from salts and proteins during the tissue regeneration process. Attachment of cells,

proteins and other biological molecules results in the formation of a dense initial coating on the surface of the implant. Following this, there is initially, formation of a hematoma resulting in the migration of mesenchymal stem cells to the defect site. Once mesenchymal stem cells have migrated to the defect and the triggering of the regeneration process has been initiated, a soft callus composed of cartilage is initially formed. The cartilage is then slowly mineralized and replaced by bone as a result of the differentiation of mesenchymal stem cells to osteoblasts and is eventually remodeled by osteoclasts, or bone resorbing cells. Irrespective of the formation of a defect, bone tissue is constantly remodeled throughout the life of an individual following birth [5-7]. Subtle variations in the homeostasis of this remodeling process lead to the occurrence of various bone diseases. The origins and roles of the three major cell types involved in the function of bone tissues will be described in the following sections.

### **1.3.1 Osteoblasts**

Osteoblasts are the cells found in bone tissue which are responsible for the formation of the organic non-mineralized bone matrix [8]. The sources for osteoblast precursor cells include mesenchymal stem cells, adipocytes, lining cells, and perivascular pericytes contiguous to a bone wound. Mature osteoblasts express proteins such as alkaline phosphatase (ALP), type I collagen (Col-1), bone sialoprotein (BSP), and osteocalcin (OCN) [9]. Due to their role in the formation of mineralized tissues, osteoblast precursor cell interaction with synthetic scaffold materials and the triggering of other mineralization signaling cascades requiring the upregulation of certain bone forming proteins and the corresponding inhibition of other non-mineralizing factors and co-factors is most often studied in the development of materials for the regeneration of mineralized tissues.

In addition to bone formation, osteoblasts secrete signaling molecules, such as osteoprotegrin (OPG), which play a key role in also regulating the resorption of mineralized tissues.

### **1.3.2 Osteoclasts**

Osteoclasts are the cells responsible for the resorption of mineralized tissues. They are derived from osteoclast precursors and hematopoietic progenitors which also give rise to both macrophages and monocytes. Mature osteoclasts form large multinucleated motile cells and are relatively rare in comparison to the other cell types found in bone. Receptor activator of nuclear factor kappa-B ligand (RANKL) is a molecule necessary for the formation of mature osteoclasts from monocyte precursor cells [10]. The interactions *in vivo* between RANKL and OPG play an important role in regulating both the resorption and formation of mineralized tissues. During resorption, osteoclast podosomes form a dense ring resulting in the formation of a sealing zone that tightly anchors the osteoclast to the mineral surface. The compartment beneath the cell is resorbed due to the acidic environment created. As a result of the harsh conditions required to resorb bone tissues, osteoclasts are capable of functioning in extremely harsh environments with an extremely low pH. [11].

### **1.3.3 Osteocytes**

Osteocytes are terminally differentiated osteoblasts which are entrapped within the bone matrix. They are the most abundant cell type found in bone. The function of osteocytes remains largely unknown since they have not been studied as much as either osteoblasts or osteoclasts. However, they have been shown to be sensitive to mechanical stimulation. As a result of their

sensitivity to mechanical stimulation, they are believed to play a role in the signaling of both, bone formation and resorption. A direct link between osteocytes and bone formation was discovered when it was observed that mature osteocytes secrete sclerostin, a potent inhibitor of bone formation. [11].

### **1.3.4 Biodegradable scaffold material types**

#### **1.3.4.1 Synthetic polymers**

Synthetic polymers are of interest for biodegradable bone scaffolds due to the capability to chemically modify their structure allowing control over degradation rate and mechanical properties. This chemical modification often leads to increased mechanical properties as compared to natural polymers. Additionally, the processes required to make synthetic polymers leads to less batch to batch variations. However, synthetic polymers are considered non-bioactive and require additional post processing steps or the addition of bioactive molecules in order to achieve the desired therapeutic effect. Some of the more common FDA approved synthetic polymers used in bone tissue engineering include poly (methyl methacrylate) (PMMA), poly(lactic-co-glycolic acid (PLGA), polycaprolactone (PCL), and polyethylene glycol (PEG) [12].

#### **1.3.4.2 Natural Polymers**

Natural polymers are either protein or polysaccharide derived and the most common used in for biodegradable scaffolds include chitosan, alginate, hyaluronic acid, silk, fibrin, and collagen. Due to their similarity to extra cellular matrix (ECM) proteins, natural polymers are considered highly biocompatible. However, due to their low mechanical properties additional plasticizers and

processing techniques are required. These additional processing techniques can lead to undesirable degradation times and some plasticizers can lead to increased cytotoxicity [12].

#### **1.3.4.3 Metals**

The alloys developed which are considered biodegradable are either Mg or Fe based, both of these elements are found within the human body. Mg is the fourth most abundant cation in the human body, playing a key role in enzymatic reactions, and is required for cell proliferation and ATP synthesis. In addition, it has recently been found to play a beneficial role on the regeneration of bone tissue.  $\text{Fe}^{2+}$  is known to be crucial in storage and activation of molecular oxygen, however the degradation of Fe based alloys results in a release of  $\text{Fe}^{3+}$  ions and causes hemoglobin to be incapable of binding oxygen. Therefore, Mg alloys are the most commonly studied degradable metal alloys for degradable bone scaffolds [13, 14].

The main limitation of Mg alloys is their rapid corrosion and degradation rate in-vivo, resulting in implant failure. Therefore, many techniques have been utilized to alter the corrosion rate of Mg alloys to enhance their capability to be used as a biodegradable alloy. These techniques will be discussed in detail in later sections.

#### **1.3.4.4 Calcium phosphate ceramics and cements**

Calcium Phosphate (CaP) Cements (CPCs) and calcium phosphate ceramics are widely used in bone tissue engineering due to their chemical similarity to the inorganic component of natural bone. CaP ceramics while most common and extensively studied tend to be very brittle when generated in the fully dense form. Typical approaches to generate CaP ceramics is by mixing the powders followed by compaction and sintering at high temperatures to a density as high as 99.9%. On the other hand, if the CaP ceramics are made porous as needed for cellular infiltration,

the mechanical properties are even more compromised. Moreover, the bulk ceramics are not amenable for molding to the desired defect shape by the clinician on demand during surgery [12, 15]. CPC's are created by mixing an aqueous liquid with calcium phosphate (CaP) precursor powders. During mixing, the precursors either undergo hydrolysis or an acid/base reaction to form a final more hydroxyapatite (HAp) or brushite phase. HAp cements are known to have mechanical properties similar to natural bone, but due to their high stability in a physiological environment, their associated degradation rate is often very high. Brushite cements on the other hand, are much less stable in physiological environments and have much shorter degradation times. However, brushite cements have lower mechanical properties and release acidic byproducts during degradation [15].

### **1.3.5 Advantages of Biodegradable scaffolds**

As discussed, prior, secondary surgeries associated with the implantation of permanent bone scaffolds gives rise to complications such as increased patient cost, longer healing times, patient discomfort, and possible risk of infections aside from inflammation. However, it is believed that the use of biodegradable scaffolds can obviate the need for additional surgeries to remove or replace permanent implants. Therefore, the work herein focuses on the study and improvement of two biodegradable scaffold systems discussed in the sections to follow.

## 1.4 Biodegradable hydroxyapatite forming calcium phosphate bone cements

### 1.4.1 Calcium phosphate (CaP) phases

The most common CaP phases used for the development of HAp forming bone cements are listed in **Table 1.3**. As discussed above, hydroxyapatite is the most stable of all the phases whereas dicalcium phosphate dihydrate (DCPD) and dicalcium phosphate anhydrous (DCPA) are the most soluble. A calcium phosphate (CaP) cement not listed above is amorphous calcium phosphate (ACP). It is regarded as having the highest solubility compared to other phases due to its lack of long-range periodicity and atomic order as well as amorphous nature. The solubility of the chosen CaP precursors is crucial in the cementing reaction described in section 1.4.2.

**Table 1.3 Types and properties of commonly used calcium phosphate phases [16].**

Abbreviation	Name	Chemical Formula	Ca/P	pK <sub>sp</sub> @ 25°C	pH Stability
TTCP	Tetracalcium phosphate	Ca <sub>4</sub> (PO <sub>4</sub> ) <sub>2</sub> O	2	38-44	-
HA	Hydroxyapatite	Ca <sub>5</sub> (PO <sub>4</sub> ) <sub>3</sub> OH	1.67	116.8	9.5-12
β-TCP	β-tricalcium phosphate	Ca <sub>3</sub> (PO <sub>4</sub> ) <sub>2</sub>	1.5	28.9	-
α-TCP	α-tricalcium phosphate	Ca <sub>3</sub> (PO <sub>4</sub> ) <sub>2</sub>	1.5	25.5	-
CDHA	Calcium deficient hydroxyapatite	Ca <sub>10-x</sub> (HPO <sub>4</sub> ) <sub>x</sub> (PO <sub>4</sub> ) <sub>6-x</sub> (OH) <sub>2-x</sub>	1.5	85.1	6.5-9.5
DCPD	Dicalcium phosphate dihydrate	CaHPO <sub>4</sub> •2H <sub>2</sub> O	1	6.59	2-6
DCP	Dicalcium phosphate anhydrous	CaHPO <sub>4</sub>	1	6.90	-

### 1.4.2 Cement setting reaction

The formation of CPCs is achieved by either hydrolysis of a precursor powder in an aqueous liquid or by an acid/base reaction between two precursor powders to form the final stable



CaP phase. After an aqueous liquid phase is added to the precursor powders a rapid dissolution of the precursors occurs resulting in a supersaturation of Ca and  $\text{PO}_4$  ions. Once the correct level of supersaturation is met, precipitation of either HAp or brushite nuclei takes place. As the reaction proceeds further, the nuclei continue to grow until a solid matrix of newly formed HAp or brushite is formed. The cementing reaction is described in detail in **Figure 1.1**. The solubility of each precursor highly dictates the rate of dissolution of the CaP precursors and ultimately the precipitation of HAp as well. A mismatch of precursor solubility can lead to unreacted precursors entrapped within the newly precipitated matrix.

Though the complete transformation of all of the precursors into the final phase can take days, the total time required for the slurry of the liquid and powders to form a solid is referred to as the “setting time”. Setting time consists of an initial and final setting time, both of which are very important clinically. The initial setting time is the amount of time required after mixing the surgeon has to mold the paste to achieve the desired shape. The final setting time is how long it takes for the cement paste to become mechanically stable enough to implant into the bone defect. Therefore, if the setting times are either too short or too long, then the cements are not able to be used clinically. The optimum initial setting time is ~8 minutes and the optimum final setting time is ~15 minutes [17].

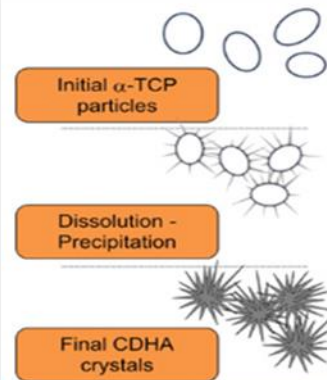
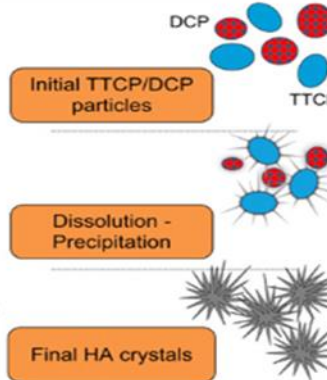
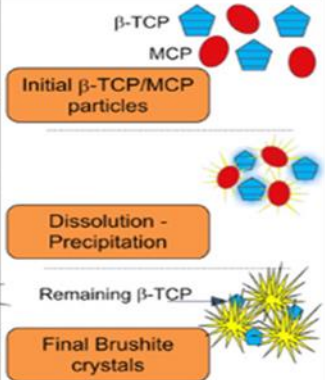
	Apatitic Cement		Brushitic Cement
	Single Component	Multiple Components	
Reactives	$\alpha$ -TCP	TTCP + DCPA/DCPD	$\beta$ -TCP + MCPM/MCPA
Reaction	$3\alpha\text{-Ca}_3(\text{PO}_4)_2 + \text{H}_2\text{O} \rightarrow \text{Ca}_9(\text{HPO}_4)(\text{PO}_4)_5(\text{OH})$	$2\text{Ca}_4(\text{PO}_4)_2\text{O} + 2\text{CaHPO}_4 \rightarrow \text{Ca}_{10}(\text{PO}_4)_6(\text{OH})_2$	$\beta\text{-Ca}_3(\text{PO}_4)_2 + \text{Ca}(\text{H}_2\text{PO}_4)_2 \cdot \text{H}_2\text{O} + 7\text{H}_2\text{O} \rightarrow 4\text{CaHPO}_4 \cdot 2\text{H}_2\text{O}$
Type of Reaction	Hydrolysis	Acid-Base	Acid-Base
Setting mechanism and crystal morphology			
			
Setting mechanism and crystal morphology			

Figure 1.1 Cementing reactions of typical calcium phosphate phases [18].

### 1.4.3 Limitations of hydroxyapatite forming calcium phosphate cements

Although HAP cements have been demonstrated to be biodegradable, osteoconductive, and osteoinductive, their application is limited by their slow degradation rates. Due to HAP's slow in-vivo degradation rate, the cements often fracture as new bone tissue is formed, resulting in a decrease in the mechanical stability of the implant. Therefore, it is crucial that new strategies are studied to decrease the solubility and degradation rate of HAP forming bone cements.

### 1.4.4 Role of strontium ions

One method to address the slow degradation rates of HAP bone forming cements is by the use of ionic substitution. In addition to Ca and P, the inorganic components of mineralized tissues

are comprised of several elements which are required for regulating function and structure (**Table 1.4**). Thus, in an attempt to further mimic the structure and composition of native mineralized tissues, the synthesis of ionic substituted HAp scaffolds for bone tissue engineering has been explored.

**Table 1.4 The elemental composition of enamel, dentin, and bone [19].**

	<b>Enamel</b>	<b>Dentin</b>	<b>Bone</b>
Ca (wt. %)	37.6	40.3	36.6
P (wt. %)	18.3	18.6	17.1
CO <sub>3</sub> (wt. %)	3.0	4.8	4.8
Mg (wt. %)	0.2	1.1	0.6
Sr (wt. %)	0.03	0.04	0.05
F (wt. %)	0.01	0.07	0.1

As of late, Sr substitution has been widely explored to adjust the HAp cement setting times, mechanical properties, as well as biocompatibility. Biologically, Sr plays a key role on the formation and remodeling of new bone. Sr stimulates osteoblast precursor proliferation and differentiation, reduces osteoclast recruitment and osteoclastogenesis, and increases apoptosis of mature osteoclasts. Recent studies on Sr substituted HAp cements have shown an increase in osteoblast proliferation and differentiation as compared to unsubstituted cements [17, 20, 21].

## 1.5 Biodegradable magnesium alloys

### 1.5.1 Corrosion mechanism

The corrosion of magnesium alloys is greatly accelerated when the metal is immersed in a simulated body fluid (SBF) containing  $\text{Cl}^-$  ions. After immersion in SBF, an initial porous  $\text{Mg}(\text{OH})_2$  passivation layer is formed on the surface of the alloy.  $\text{Cl}^-$  ions from the SBF then begin to adsorb onto the passivation layer and allow the formation of  $\text{MgCl}_2$  precipitates. Due to the relatively high solubility of  $\text{MgCl}_2$ , the  $\text{MgCl}_2$  precipitates dissolve into the solution and pits of bare alloy begin forming. These pits eventually connect and lead to large fragments of the Mg alloy breaking off from the bulk alloy. During the corrosion process, released  $\text{OH}^-$  ions cause the pH of the solution to increase and  $\text{H}_2$  gas is released. When implanted in-vivo, the released  $\text{H}_2$  gas can lead to gas pockets causing cellular and tissue detachment from the alloy [12]. The corrosion reaction and the process is shown in detail in **Figure 1.2**. Therefore, in order to prevent the rapid corrosion of Mg alloys numerous surface techniques have been utilized to retard the corrosion kinetics. These techniques can be classified as conversion reactions or deposition reactions involving inorganic, organic, anodizing, hydride coatings as well as vapor phase processes. The process that was followed in this thesis is metal arc oxidation (MAO) as one of the chemical conversion approaches which is described below and in the remaining sections of this thesis.

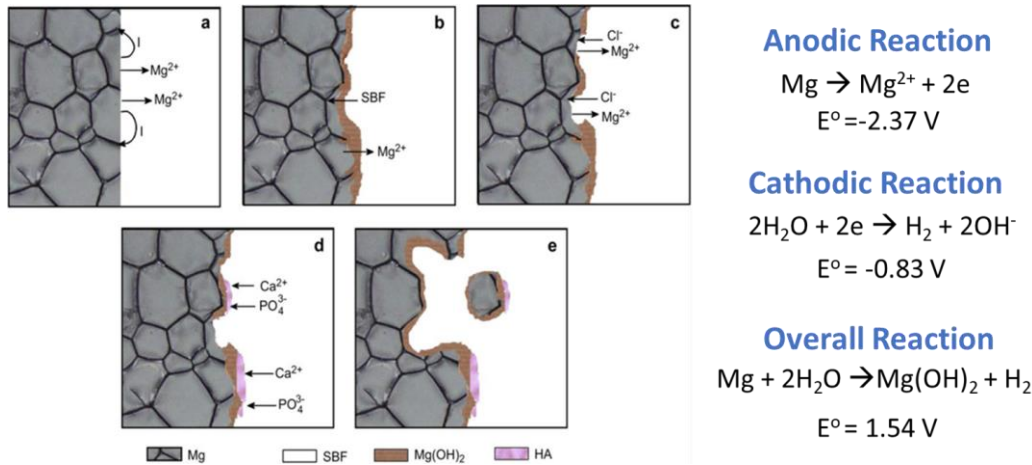


**Figure 1.2** Schematic diagram and associated reactions during the corrosion of Mg alloys in simulated body fluid (SBF) [22].

### 1.5.2 Micro-arc oxidation coating

In order to reduce the high corrosion rate associated with Mg alloys, numerous surface treatments have been studied. The main surface treatment methods are shown in **Table 1.5**. Biomimetic coatings are deposited by immersing metallic substrates in solutions containing  $\text{Ca}^{2+}$  and  $\text{PO}_4^{3-}$  ions kept at physiological temperatures for extended periods of time, however the coatings formed are normally porous and are poorly adhered to the alloy. Organic sol-gel based methods have shown to provide increased corrosion resistance, but the coatings formed are often times only stable for a few weeks. Additionally, sol-gel based methods require high temperature post treatments that are not suitable for Mg alloys. Plasma assisted methods tend to create very dense, homogenous, and highly adhered coatings. However, it is very difficult to create coatings on complex 3D shaped substrates due to the line of sight needed for the coating process [13, 14].

**Table 1.5 Advantages and disadvantages of various surface treatment methods used to reduce corrosion of Mg alloys.**

<b>Coating Technique</b>	<b>Advantages</b>	<b>Disadvantages</b>
<b>Aqueous Biomimetic Methods</b>	Can be performed under physiological conditions. Capable of incorporating biological molecules during the coating process. Coatings can be deposited on porous 3D scaffolds.	Coating process requires relatively long periods of time. Acidic or basic pretreatment is often required. Coating adhesion is relatively poor.
<b>Organic Sol-Gel Based Methods</b>	Coatings can be deposited on porous 3D scaffolds. Homogeneous coatings can be formed using techniques such as dip or spin coating. The coating process is relatively quick.	Heat treatment to decompose organic precursors is required. Therefore, biological molecules cannot be simultaneously incorporated.
<b>Electrochemical Methods</b>	Coatings can be deposited on porous 3D scaffolds. High temperature processing and alloy pretreatments are not required. Coatings can be deposited very quickly.	Coating adhesion to the substrate is relatively poor without heat treatment.
<b>Plasma Assisted Methods</b>	Very homogeneous and dense coatings with excellent adhesion to the substrate can be formed. Coatings are deposited relatively quickly. Coating crystallinity can be easily adjusted.	Cannot be used to coat 3D porous scaffolds due to line of sight deposition. Coating deposition is often performed under vacuum conditions at elevated temperatures.

One type of electrochemical coating process that has been widely studied for producing highly stable corrosion resistant coatings on Mg alloys is micro-arc oxidation (MAO). MAO is a high voltage anodic oxidation process that utilizes plasma arc discharges, extreme local temperatures, and a conductive electrolyte to produce highly tunable ceramic coatings. The produced oxide consists of a thin interfacial layer between the alloy and oxide, a dense inner layer, and a porous outer layer (**Figure 1.3**). The composition of the formed oxide layer, layer thickness, porosity, and resulting corrosion resistance can be altered by the various MAO processing parameters. Vladimir et al. has shown that an MAO coating deposited on AZ91D Mg alloys significantly reduced the corrosion rate when immersed in a 3% NaCl solution (**Figure 1.4**) [23]. Additionally, the porous nature of the outer layer of the MAO coating has been utilized for delivery of antibiotics and growth factors in-vitro [24, 25].

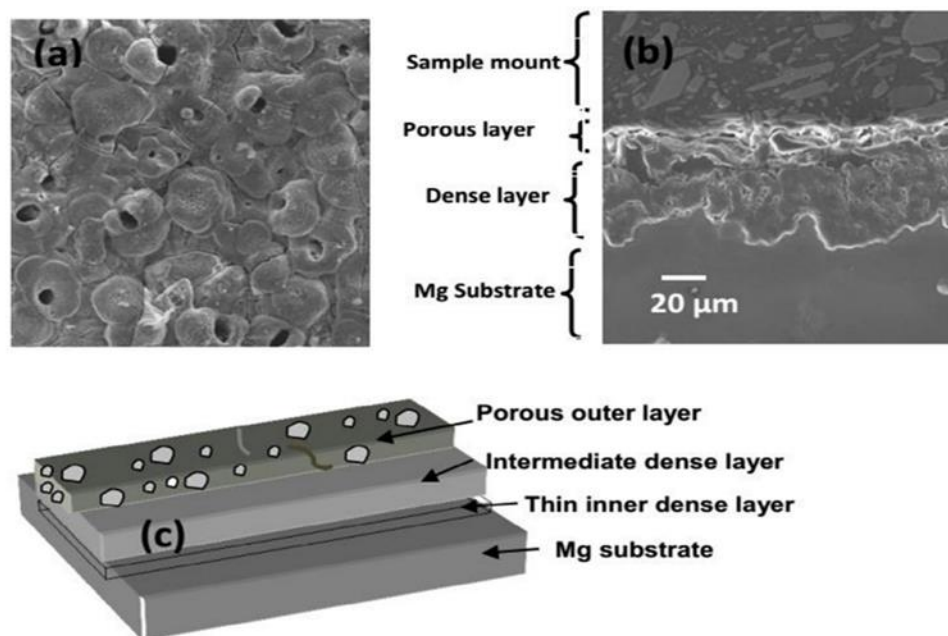


Figure 1.3 Schematic diagram of the surface and cross section of micro-arc oxidation coatings [26].

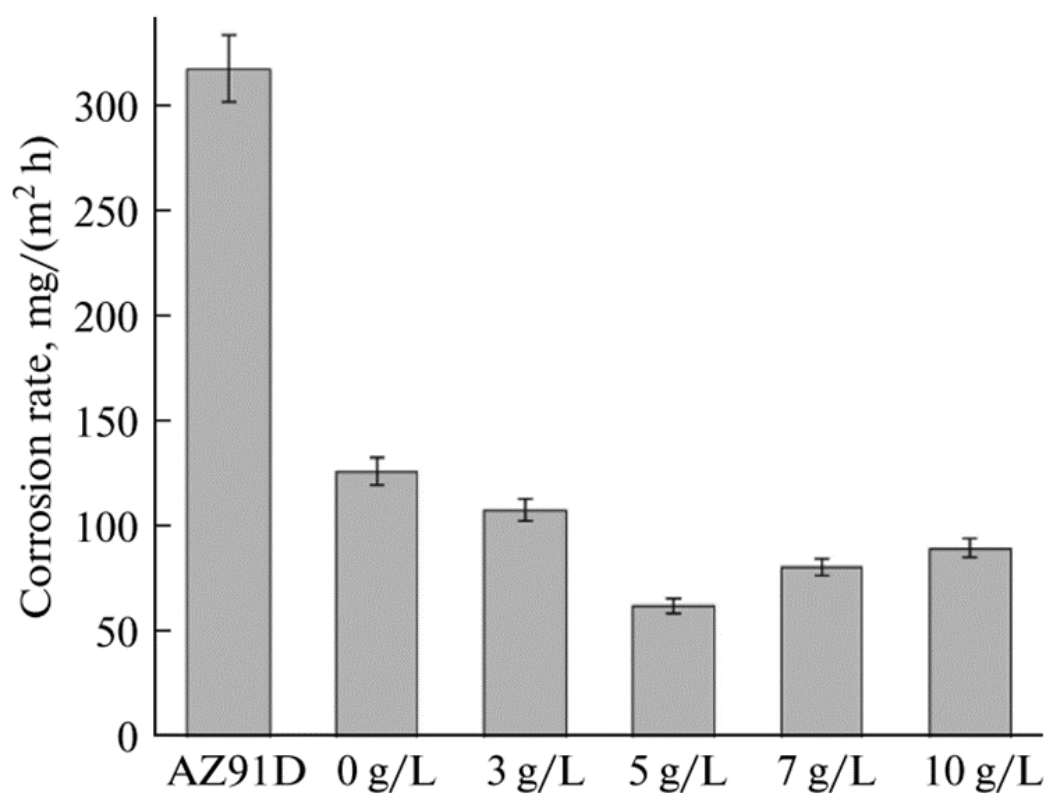


Figure 1.4 Corrosion rate of bare and MAO coated AZ91D in a 3% NaCl solution at 37°C [23].

## **2.0 Thesis goals**

### **2.1 Specific aim 1**

#### **Biodegradable Bioceramic Micro-Arc Oxidation Coating on Lithium-Aluminum-Zinc (LAZ) and Lithium-Zinc (LZ) Magnesium Alloys**

**Hypothesis:** In-vitro corrosion of bare LAZ and LZ alloys results in a large burst release of ions from the alloys leading to in-vitro cytotoxicity. Micro-arc oxidation of these alloys will provide a barrier to the surrounding environment coming in contact with the bare alloy resulting in the alloys exhibiting a more controlled and reduced corrosion rate. Therefore, by decreasing the large burst release of ions during degradation, the cytocompatibility of the alloys should be increased.

#### **Goals:**

1. Understand the role Li and Al alloying elements in the alloys play on the materials properties and corrosion resistance of the produced MAO coating.
2. Evaluate how the increased corrosion resistance of the MAO coatings affects the in-vitro cytocompatibility of the coated alloys.



## 2.2 Specific Aim 2

### **Resorbable Strontium Substituted Amorphous Calcium Phosphate and Dicalcium Phosphate Dihydrate Based Hydroxyapatite Forming Bone Cement**

**Hypothesis:** Synthesized amorphous calcium phosphate (ACP) and Sr substituted dicalcium phosphate dihydrate (SrDCPD) were chosen as precursors for generating a stable nanoHA forming cement. Rapid hydrolysis of ACP to nano-HAp will enable the cementing reaction to occur at room temperature while the slower hydrolysis of DCPD will allow for incorporation of  $\text{Sr}^{2+}$  ions within the HAp lattice resulting in sustained release of  $\text{Sr}^{2+}$  ions. The dissolution of  $\text{Sr}^{2+}$  will increase the in-vitro attachment and proliferation of murine preosteoblast MC3T3-E1 cells.

#### **Goals:**

1. Understand the effect of Sr ions on the cementing reaction and overall cement materials and mechanical properties.
2. Understand the effect of Sr on the ion release during in-vitro dissolution tests of the resultant cements.
3. Understand the effect of Sr on the in-vitro cytocompatibility of the resultant cements.

### **3.0 Biodegradable Bioceramic Micro-Arc Oxidation Coating on Lithium-Aluminum-Zinc (LAZ) and Lithium-Zinc (LZ) Magnesium Alloys**

#### **3.1 Introduction**

One alloy that our group has focused on primarily as a candidate biodegradable magnesium alloy is magnesium (Mg) alloyed with lithium (L), aluminum (A), and Zinc (Z). The corresponding LAZ and LZ alloy systems have been shown to possess ultra-high ductility (UHD), but can be limited in application due to their cytotoxicity related to the high corrosion rate which varies by elemental composition of the alloy [27]. Due to the presence of multiple phases within both LAZ and LZ alloys, galvanic corrosion due to the varying corrosion potentials of the individual phases lead to increased corrosion rates. Thus, the goal of this thesis work is to attempt to reduce the corrosion rate of the LAZ and LZ alloy systems in order to increase their effectiveness as biodegradable biomaterials for treating bone defects and injuries.

In order to reduce corrosion of the LAZ and LZ alloys a MAO coating technique will be utilized to form a corrosion resistant layer on the surface of the alloys. The chosen electrolyte that the Mg alloy is immersed in during MAO coating plays a major role on the composition and structure of the coating. [128 bara] et al. showed that the presence of KF in the electrolyte solution during the MAO coating of AZ91 resulted in a highly dense inner layer and significantly increased corrosion resistance. Addition of silicates within the electrolyte solution resulted in the formation of silicate containing oxides and therefore, increased the stability of the deposited coatings during immersion in SBF. Lastly, the presence of phosphates within the electrolyte solution formed coatings that were thicker and exhibited increased cytocompatibility as compared to ZK60

magnesium alloys coated without the presence of phosphates. Therefore, the composition of the electrolyte used in this study included fluorides, phosphates, and silicates in order to make a dense, corrosion resistant, and cytocompatible MAO coating.

In addition to the electrolyte components, the alloying elements of the MAO coated alloy can affect the deposited coatings by the formation of additional phases containing the alloying elements. Therefore, the effect of the alloying elements, Li and Al, on the morphology, phase composition, corrosion protection, and cytocompatibility of the coatings was studied.

## **3.2 Materials and methods**

### **3.2.1 Substrate preparation**

Two Mg-Li-Al-Zn alloys of nominal composition (wt.%) of Li, Al, and Zn, respectively, Mg-6Li-3Al-1Zn (LAZ631) and Mg-9Li-3Al-1Zn (LAZ931) and two Mg-Li-Zn alloys of nominal composition (wt.%) Li and Zn, respectively, Mg-6Li-1Zn (LZ61) and Mg-9Li-1Zn (LZ91) were acquired from Zi'an SiFang EM Co., LTD (Zi'an, China). Each alloy was generated by conventional melting and casting procedures followed by extrusion to 20mm diameter rods. Circular discs were machined down from the extruded rods to a thickness of 1.0 mm and diameter of approximately 15mm. The machined samples then underwent a degreasing step by acid etching in 3% HNO<sub>3</sub> followed by rinsing in acetone, as previously described [28-30]. The samples were then polished using SiC polishing paper sequentially up to 4000 grit (Allied High Tech Products Inc., Compton, CA). After polishing, the samples were sonicated in acetone for 30 minutes and then stored in fresh acetone until further testing and coating.

### **3.2.2 Micro-arc oxidation coating**

Prior to coating, a 1 mm hole was drilled into the edge of the cleaned alloy sample. During MAO coating, a titanium wire was attached to the power supply and used to suspend the sample via the drilled hole. The electrolyte solution used for MAO was prepared using 8 g l<sup>-1</sup> Na<sub>2</sub>SiO<sub>3</sub> (Alfa Aesar, Ward Hill, MA), 6 g l<sup>-1</sup> Na<sub>3</sub>PO<sub>4</sub>, and 4 g l<sup>-1</sup> KF (Sigma Aldrich, St. Louis, MO) and stored at 4°C prior to usage. Prior to MAO coating, approximately 2 L of the electrolyte solution was poured into a stainless-steel container that was chilled with an ice bath. The prepared sample was connected as the anode and the stainless-steel container was connected as the cathode to the power supply (TDK Lambda, GEN 2400W). A current of 229 mA and potential between 335 to 345 V was applied for a 10-minute period. The MAO coated samples were then rinsed in deionized water and ethanol, and were subsequently dried at room temperature

### **3.2.3 Electrochemical corrosion testing**

Prior to potentiodynamic polarization tests (PDP) electrical contacts with the cleaned samples were prepared. A conductive silver paste was applied to the back of the samples and a 24-gauge electrical wire was placed between the sample and conductive silver paste. The paste was allowed to set for 72 hours at room temperature. An epoxy resin (EpoxyCure, Buehler, Lake Bluff, IL) was then applied to cover the entire back of the sample and silver epoxy to provide insulation and was allowed to set for 24 hours. PDP experiments were performed using a CHI 604A instrument (CH Instruments, Inc., Austin, TX). A 3-electrode cell set-up was used, with the prepared coated and uncoated substrates, an Accumet Ag/AgCl reference electrode (Fischer Scientific), and a platinum wire serving as the working, reference and counter electrodes

respectively. *In vitro* conditions were mimicked by using the Hank's balanced salt solutions as the electrolyte solution that was maintained at 37°C (**Table 3.1**). Prior to PDP testing, the open circuit potential was analyzed over a 30-minute period to establish the equilibrium potential of the system. The PDP tests were performed at a voltage range designated by 0.2 V below the OCP and 0.5V above the OCP using a scan rate of 1 mV/s. The TAFEL data collected was used in conjunction with linear extrapolation to estimate the corrosion current ( $I_{corr}$ ) and corrosion potential ( $E_{corr}$ ) of the bare and MAO coated LAZ631, LAZ931, LZ61, and LZ91. The estimated corrosion rate ( $CR_{corr}$ ) was calculated following ASTM-G102-89 using the equation below.:

$$C_{corr} = \frac{I_{corr}KEW}{\rho A} \quad (3-1)$$

Where  $C_{corr}$  is the corrosion rate in mmpy,  $I_{corr}$  is the corrosion current density in  $\mu A/cm^2$ , the constant K is  $3.272 \times 10^{-2}$ , EW is the equivalent weight in g/equivalent,  $\rho$  is the density of the material in  $g/cm^3$ , A is the area of the material in  $cm^2$ .

**Table 3.1 Components of Hank's Balanced Salt Solution**

Components	g/L
Calcium chloride (anhydrous)	0.1396
Magnesium sulfate (anhydrous)	0.09767
Potassium Chloride	0.4
Potassium phosphate monobasic (anhydrous)	0.06
Sodium chloride	8
Sodium phosphate dibasic (anhydrous)	0.04788
D-glucose	1

### 3.2.4 In-vitro static immersion degradation testing

*In vitro* static degradation testing was conducted on MAO coated LAZ631, LAZ931, LZ61, and LZ91. The immersion degradation experiments were conducted in accordance with ASTM

F3268 and NACE TMO169/ASTM G31-12A. In brief, MAO coated alloys were immersed and suspended within a closed system consisting of Hank's balanced salt solutions (**Table 3.1**) as the electrolyte and maintained at 37°C. A solution volume to surface area ratio of 20 mL: 1cm<sup>2</sup> was used. The experiment was conducted for 5 weeks, and at each time point (1, 3, and 5 weeks) the sample was removed from the solution, air dried, and stored in a desiccator until further materials characterization. At each time point the immersion solution was collected, acclimated to room temperature and the pH was measured. The solutions were then stored at 4°C for further analysis.

### **3.2.5 Coating characterization**

The phase composition and crystallinity of the MAO coatings were characterized using X-ray diffraction (X-Pert PRO Cu K $\alpha$   $\lambda$ =1.5418Å, with X'celerator detector, Philips). During measurements, the X-ray generator was operated at 45 kV and 40 mA and the data was collected between 2 $\theta$  values of 10-90°. Assessment of the microstructure of the MAO coated samples prior to degradation testing as well as corroded samples was conducted using scanning electron microscopy (SEM; JSM6610LV, JEOL). The samples were sputtered coated with palladium using a Cressington 108a sputter coater prior to imaging. The elemental composition of the surface of the MAO coatings was analyzed with energy dispersive X-Ray spectroscopy (EDX).

### **3.2.6 Ion release measurements**

The ions released from the MAO coated alloys during immersion degradation were assessed by inductively coupled plasma-optical emission spectroscopy (ICP-OES, iCAP duo 6500 Thermo Fisher). In order to remove any possible precipitates from the collected solutions, the

solutions were diluted 10X by adding 9mL of 3% HNO<sub>3</sub> to 1mL of the collected solutions. A standard calibration curve was generated by using known Mg, Li, Al, and Zn elemental standards diluted in 3% HNO<sub>3</sub> to the desired concentration range. The standard calibration curve was used to evaluate the amounts in ppm of each desired element within the solution.

### **3.2.7 Mouse preosteoblast cell (MC3T3-E1) culture**

Murine preosteoblast cell line, MC3T3-E1, was obtained from ATCC (Manassas, VA). The cells were cultured in minimum essential medium alpha ( $\alpha$ -MEM, Gibco, Grand Island, NY) containing 10% FBS and 1% penicillin streptomycin (P/S, Gibco, Grand Island, NY) at 37°C in 5% CO<sub>2</sub> and 95% relative humidity. Cells collected after their 4<sup>th</sup> passage were used in the experiments and seeded at a density of 50,000 cells per sample. Prior to cell seeding, all samples were UV sterilized and growth media was changed daily.

### **3.2.8 Live/dead staining**

The attachment and proliferation of MC3T3-E1 cells seeded directly on the MAO coated LAZ631, LAZ931, LZ61, and LZ91 alloys was assessed by live/dead staining (Invitrogen, Live/Dead staining kit) after 1 and 3 days of cell culture in growth media. At days 1 and 3 of culture the samples were rinsed twice with phosphate buffered saline (PBS) and incubated in PBS containing the live/dead stain for 30 minutes. The PBS containing the live/dead stain was removed and replaced with fresh PBS. Imaging was conducted using an Olympus CKX41 fluorescent microscope. The imaged samples were then prepared for SEM imaging by fixation using 2.5%

glutaraldehyde and then progressive ethanol dehydration. The samples were then sputter coated and imaged using SEM as described above.

### **3.2.9 Direct MTT assay**

Cell viability of cells directly seeded on the MAO samples was assessed using the MTT activity assay (Vybrant MTT Cell Proliferation Assay Kit). The cells were subjected to 500  $\mu$ L of fresh growth media consisting of minimum essential medium alpha ( $\alpha$ -MEM, Gibco, Grand Island, NY) containing 10% FBS and 1% penicillin streptomycin (P/S, Gibco, Grand Island, NY) and 50 $\mu$ L of 12mM (3-(4,5-Dimethylthiazol-2-yl)-2,5-diphenyltetrazolium bromide) solution and incubated for 4 hours. After incubation, 500  $\mu$ L of sodium dodecyl sulphate was added and incubated for 18 hours to solubilize the formazan. After 18 hours, 200  $\mu$ L of each sample's solution was transferred to a 96 well plate and the absorbance of the sample was measured using Synergy2 Multi-Mode Microplate Reader (Biotek, USA) with an emission wavelength of 570nm.

## **3.3 Results**

### **3.3.1 Materials characterization of MAO coated LAZ and LZ alloys**

Alloy composition is one of the major factors that affects the surface morphology and elemental composition of the synthesized MAO coating. Thus, in order to examine the effect of alloy composition on the coatings, SEM and EDX elemental analysis were performed on each of the MAO coated LAZ631, LAZ931, LZ61, and LZ91 and displayed in **Figure 3.1**. SEM images



reveals that the coatings on each of the 4 alloys contain characteristic pores ranging from ~0.5 to 30  $\mu\text{m}$  in size created by the plasma arc discharges involved in generating the MAO coatings. Within the Al containing alloys, an increase of 3 wt.% Li results in less total pores as well as the presence of cracks on the surface of the coating (**Figure 3.1 (a, b)**). This effect is not seen in the non-Al containing alloys. When comparing MAO coatings of alloys with the same amount of Li, the addition of Al results in a decrease in the overall pore size. EDX confirms the presence of Mg, Al, and Zn within the MAO coated LAZ alloys and Mg, and Zn as expected on the LZ alloys, thus confirming the participation of the alloying elements in the MAO coating process. EDX analysis also confirms that the MAO coating on each alloy consists mainly of Mg, O, Si, P, and C, but the amount of each varies depending on the Li and Al content of the alloy. The highest amount of elemental Si was detected in the MAO coated LAZ631 (19.02 wt.%) and the least on MAO coated LZ91 (9.47 wt.%) (**Figure 3.1 (a)**). Further analysis reveals that the addition of Al increases the Si content within the coating, whereas higher amounts of Li decreases the Si content (**Figure 3.1**).

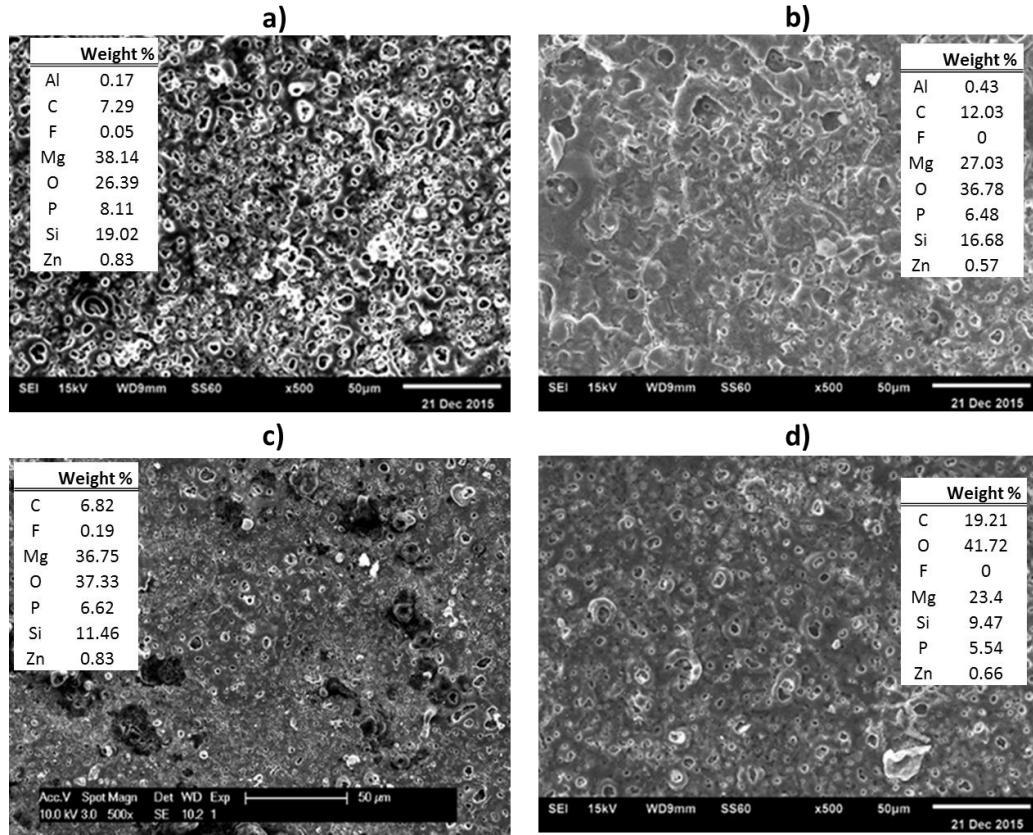


**Figure 3.1** SEM microstructure and EDX elemental composition of MAO coatings on a) LAZ631, b) LAZ931, c) LZ61, d) LZ91

MAO coatings can consist of amorphous as well as crystalline phases. In order to examine the phases present in the MAO coatings, XRD was performed on each of the coated and uncoated alloys and the X-ray patterns are displayed in **Figure 3.2**. XRD patterns of coatings on non-Al containing alloys, LZ61 and LZ91, reveals the characteristic peaks of crystalline MgO and  $\text{Mg}_2\text{SiO}_4$ . XRD patterns of coatings on LAZ631 and LAZ931 not only shows the characteristic peaks of MgO and  $\text{Mg}_2\text{SiO}_4$  ( $2\text{MgO} \cdot \text{SiO}_2$ ), but characteristic peaks of  $\text{AlPO}_4$  ( $0.5\text{Al}_2\text{O}_3 \cdot 0.5\text{P}_2\text{O}_5$ ) and  $\text{LiAlSi}_4\text{O}_{10}$  ( $0.5\text{Li}_2\text{O} \cdot 0.5\text{Al}_2\text{O}_3 \cdot 4\text{SiO}_2$ ) are also detected due to the presence of Al in the alloys.

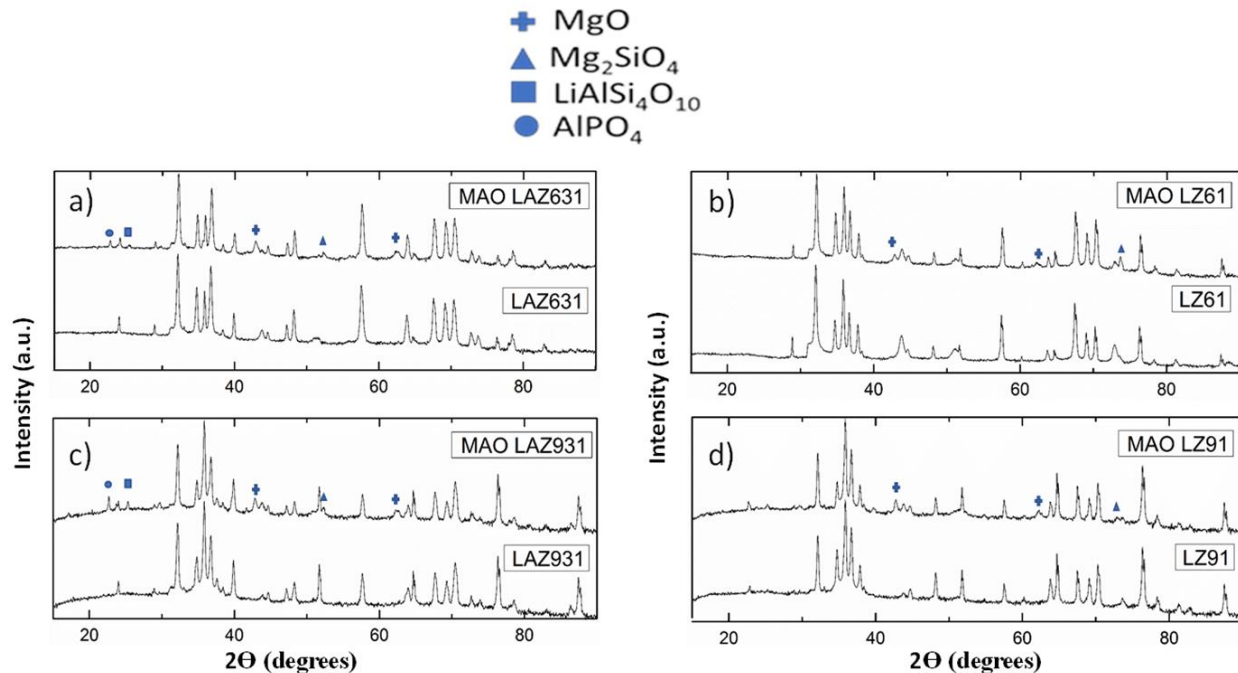
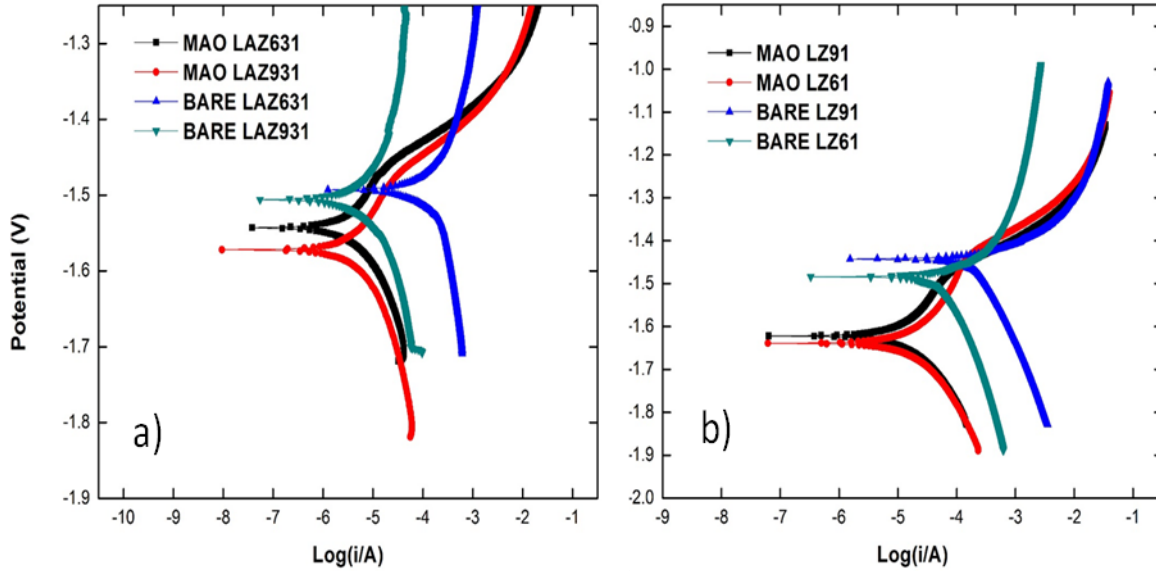


Figure 3.2 XRD diffraction pattern of bare and MAO coated substrates a) LAZ631, b) LZ61, c) LAZ931, and d) LZ91

### 3.3.2 In-vitro degradation of MAO coated LAZ and LZ alloys

The major role of the MAO coatings was to decrease the overall corrosion and degradation of the LZ and LAZ alloys of Mg. Thus, in order to determine the ability of the MAO coating to decrease corrosion, in-vitro immersion and electrochemical tests were correspondingly performed in HBSS maintained at 37°C. **Figure 3.3** depicts the potentiodynamic polarization (PDP) curves of the coated and non-coated LAZ631, LAZ931, LZ61, and LZ91 alloys and **Table. 3.2** displays the calculated  $E_{\text{corr}}$ ,  $I_{\text{corr}}$ , and  $CR_{\text{corr}}$ . Results reveal that the MAO coatings caused an overall decrease in the corrosion current density as compared to their bare alloy, thus leading to a decrease in the corrosion rate. Amongst the MAO coated samples, LAZ631 displayed the lowest corrosion rate ( $0.051 \pm 0.019$  mm/year) whereas LZ61 displayed the highest corrosion rate ( $0.274 \pm 0.065$  mm/year).

mm/year) (**Table 3.2 b**). MAO coated LAZ alloys of Mg displayed a significantly lower corrosion rate compared to MAO coated LZ alloys of Mg ( $p < 0.05$ ). No such trend was observed due to the content of Li within the groups.



**Figure 3.3** Potentiodynamic polarization data collected from coated and uncoated a) LAZ631 and LAZ931 and b) LZ61 and LZ91 within Hank's balanced salt solutions maintained at 37°C. N=4

In order to further assess the corrosion protection and stability of the MAO coatings over time, an in-vitro static immersion test was performed in HBSS maintained at 37°C for 5 weeks. **Figure 3.4** depicts the release of Mg, Li, and Al ions from the MAO coated samples during the immersion test as well as the pH of the immersion solutions. After 1 week of immersion in HBSS, there is no significant difference in Mg and Al ion release among the samples. However, the MAO coated LZ91 alloy shows a significantly higher release of Li as compared to MAO coated LAZ631 ( $p < 0.05$ ). At 3 weeks of immersion, the MAO coating on LZ91 begins to further degrade as indicated by an increase in the released ions. At this time point, the concentration of Mg ions within the solutions containing MAO coated LZ91 is significantly higher than MAO coated LAZ631,

LAZ931, and LZ61 ( $p < 0.05$ ). Furthermore, the amount of Li ions as expected, within the immersion solution for MAO coated LZ91 and LAZ931 is significantly higher than the MAO coated LAZ631 and LZ61 ( $p < 0.05$ ). The same trend seen at week 3 for MAO coated LAZ931 and MAO coated LZ91 is observed after 5 weeks of immersion as well. At each time point, there is no significant difference in the ion release between MAO coated LAZ631 and LZ61 as well as Al ion release between MAO coated LAZ631 and LAZ931 except for week 5 for Al ion release. Thus, we can conclude that an increase in the Li content in the alloy leads to a less stable MAO coating over time, as seen in the MAO coated LZ91 and LAZ931. However, at higher Li contents, the addition of Al aids in stabilizing the produced MAO coatings as observed between the MAO coated LAZ931 and LZ91 at week 3 and 5 of immersion. The pH measurements of the immersion solutions also reveal a similar trend. The pH of the solutions for all the MAO coated samples after 1-week immersion are all in the ranges of 8.5 – 9. However, as the MAO coating on LZ91 begins to degrade more rapidly than the others, the pH becomes significantly higher than the other three samples after 3 and 5 weeks immersion ( $p < 0.05$ ).

**Table 3.2** Calculated corrosion potential, current density, and corrosion rate from PDP measurements of a) uncoated alloys and b) coated alloys

<b>a)</b>			
	$E_{corr}$ (V)	$i_{corr}$ (log(A/cm <sup>2</sup> ))	CR <sub>corr</sub> (mm/year)
LAZ631	-1.51 ± 0.03	-3.81 ± 0.64	1.57 ± 0.11
LAZ931	-1.51 ± 0.01	-4.94 ± 0.19	0.30 ± 0.12
LZ61	-1.52 ± 0.02	-4.56 ± 0.85	1.14 ± 0.94
LZ91	-1.46 ± 0.01	-3.87 ± 0.15	3.45 ± 1.21

<b>b)</b>			
	$E_{corr}$ (V)	$i_{corr}$ (log(A/cm <sup>2</sup> ))	CR <sub>corr</sub> (mm/year)
MAO LAZ631	-1.54 ± 0.04	-5.69 ± 0.20	0.051 ± 0.019
MAO LAZ931	-1.54 ± 0.07	-5.48 ± 0.23	0.088 ± 0.037
MAO LZ61	-1.65 ± 0.03	-4.96 ± 0.10	0.274 ± 0.065
MAO LZ91	-1.58 ± 0.04	-5.16 ± 0.11	0.178 ± 0.046

In order to visualize the surface morphology and analyze the elemental composition of the degradation products, SEM images and EDX was performed after 5 weeks of immersion and is displayed in **Figure 3.5**. SEM images of MAO coated LAZ631, LAZ931, and LZ61 after 5 weeks immersion, **Figure 3.5 (a-c)** respectively, reveal similar morphology and characteristic MAO micro pores as seen in **Figure 3.1** of the freshly coated samples. However, the presence of numerous large cracks spanning throughout the surface is due to the degradation of the coatings within the HBSS solution. SEM image of MAO coated LZ91 (**Figure 3.5 (d)**) reveals very little of the original MAO surface morphology characteristics and instead reveals surface morphology similar to the corroded alloy. Thus, we can conclude that only the MAO coatings on LAZ631, LAZ931, and LZ61 are stable up to 5 weeks immersion in HBSS. Further analysis via EDX reveals the elemental composition of degradation products and precipitates on the surface of the coatings primarily consists of Ca, Mg, O, and P. However, the surface of MAO coated LAZ631, LAZ931,

and LZ61 have much higher amounts of Ca and P and lower amounts of O as compared to MAO coated LZ91. This is attributed to the instability of the MAO coating on LZ91 and the larger amount of corrosion that is taking place on the surface of the alloy. Lastly, the coated alloy with the highest amount of Si detected on the surface after 5 weeks immersion is LAZ631 (**Figure 3.5 (a)**).

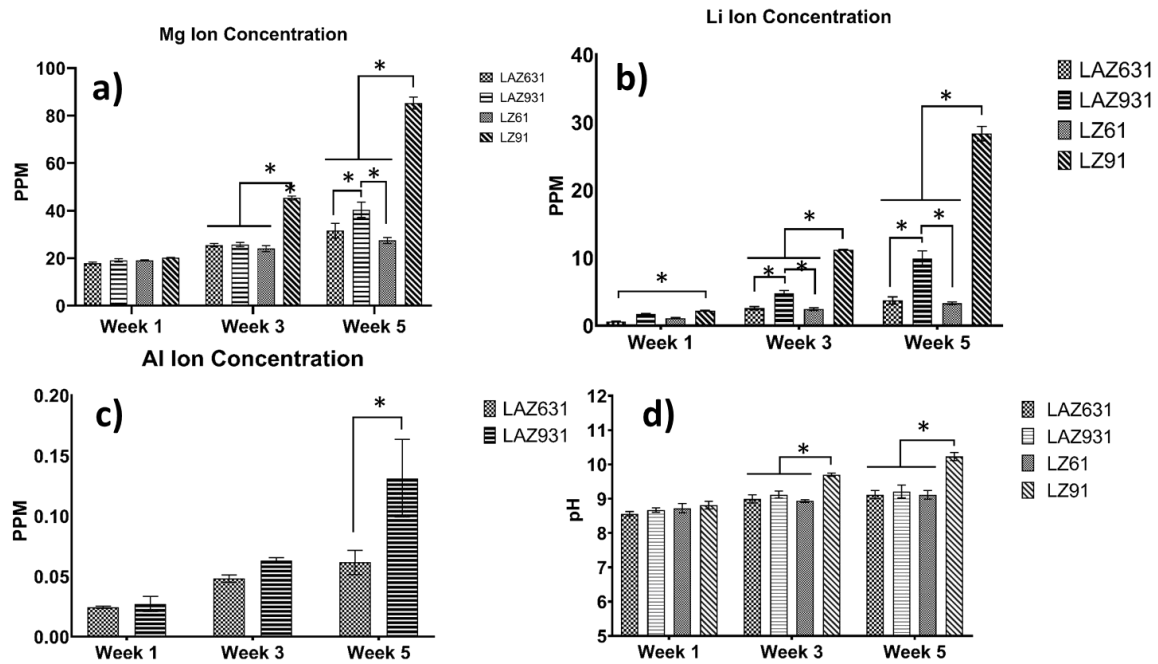
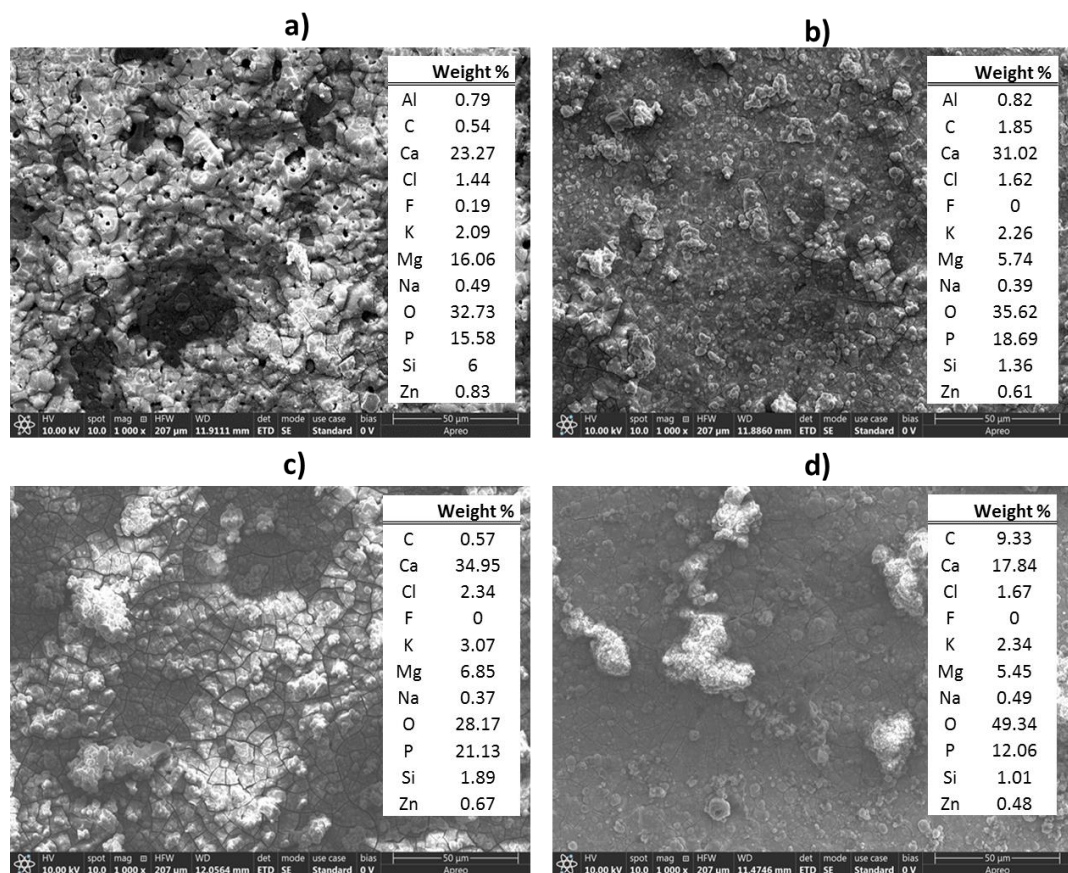


Figure 3.4 a) Mg, b) Li, c)Al ions released and d) solution pH measurements during static immersion testing in Hank's balanced salt solution maintained at 37°C. N=3, significance determined by  $p < 0.05$ .





**Figure 3.5** Microstructure and elemental composition of MAO coatings on a) LAZ631, b) LAZ931, c) LZ61, and d) LZ91 after 5 weeks immersed in Hank's balanced salt solution maintained at 37°C.

### 3.3.3 In-vitro cytocompatibility of MAO coated LAZ and LZ alloys

In order to evaluate the ability of the MAO coated LAZ and LZ alloys to allow for cellular attachment and proliferation a Live/dead staining was performed after 1 (**Figure 3.6**) and 4 days (**Figure 3.7**) of culture and examined by optical microscopy to view the live cells stained green and the dead cells stained red. **Figure 3.6** reveals that after day 1 of culture in growth media, live cells were only detected on the positive control (tissue culture plastic) and on the MAO coated LAZ631 alloy. All the cells were found to be dead on the MAO coated LZ61, LZ91, and LAZ931 alloys. Due to this observation, only the MAO coated LAZ631 was continued for further



cytocompatibility analysis. **Figure 3.7** reveals that after day 4 of culture, dead cells, hydrogen gas bubbles, as well as large areas with no cellular attachment was detected on the MAO coated LAZ631 alloy. Following live/dead staining, cells were fixed on the MAO coated LAZ631 alloy and imaged using SEM (**Figure 3.7 c**). Presence of multiple cells spanning many micro pores present on the surface of the MAO coated alloy is seen. These results suggest that the pore sizes created during the MAO process did not negatively affect cellular attachment and proliferation.

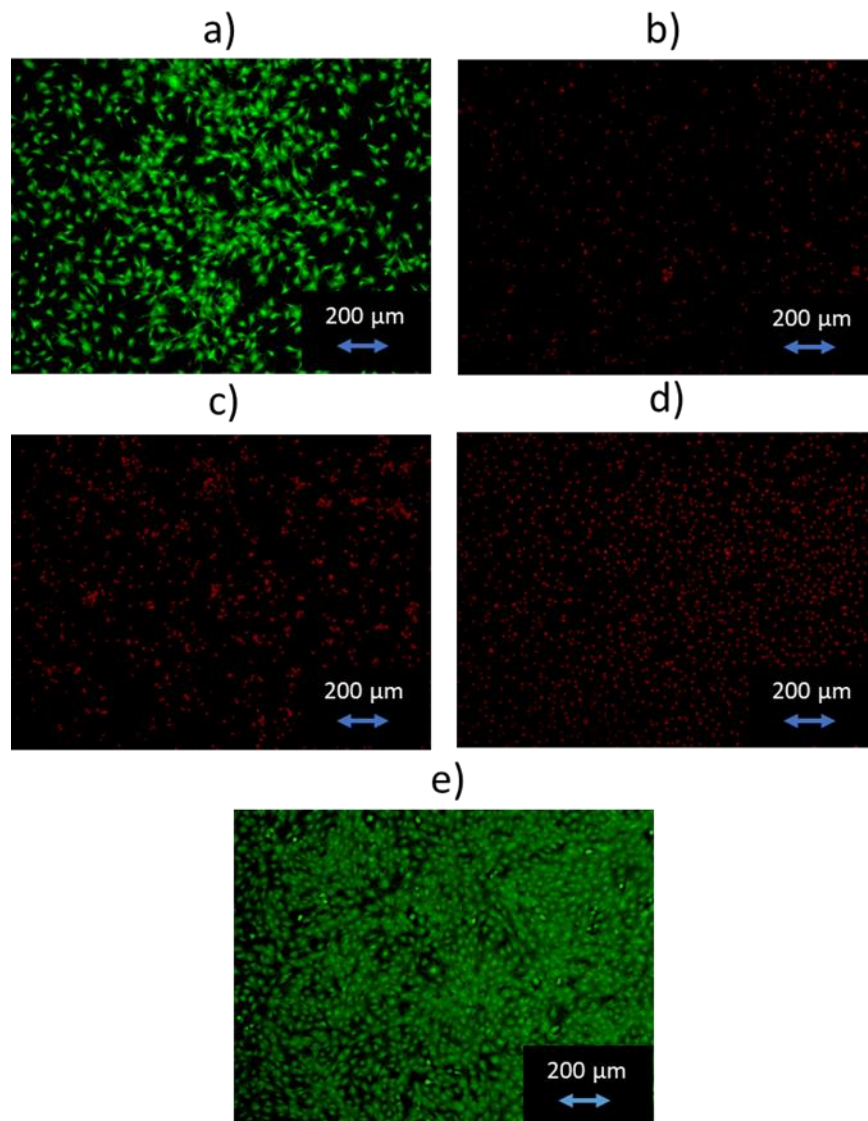


**Figure 3.6** Live/dead staining of MC3T3-E1 cells after 1 day culutre in growth media on MAO coated a) LAZ631, b) LAZ931, c) LZ61, d) LZ91, and e) tissue culture plastic ( + control).

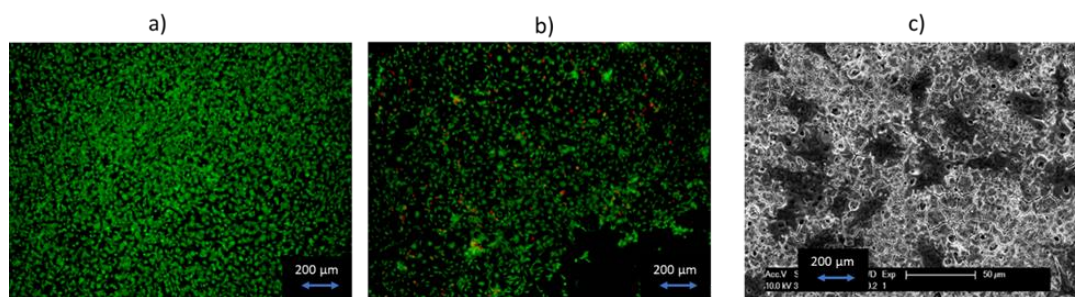


**Figure 3.7** Live/dead staining of MC3T3-E1 cells after 4 days of culture in growth media on a) tissue culture plastic ( + control), b) MAO coated LAZ631, and c) SEM image of fixed cells on the surface of MAO coated LAZ631 after 4 days of culture in growth media.

In order to quantitatively evaluate the cytocompatibility of the MAO coated LAZ631 alloy, a direct MTT assay was performed after day 1, day 4, and day 7 of culture (**Figure 3.8**) in growth media. As seen in the Live/Dead assay, the cell viability is highest after 1 day of culture and then significantly decreases at days 4 and 7 ( $p < 0.05$ ), respectively. As discussed, this can be attributed to the inability of the porous MAO coating to fully prevent corrosion of the underlying alloy even at early time points.

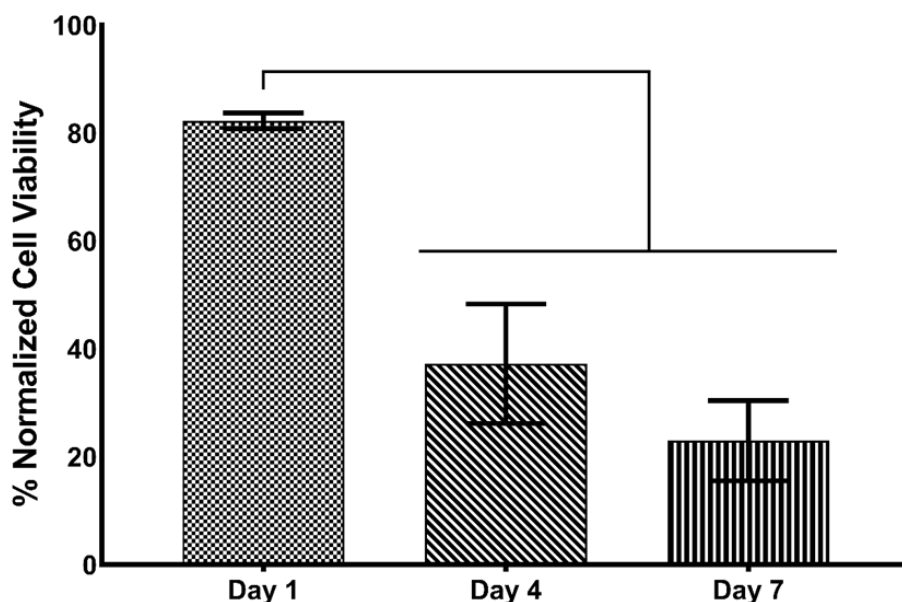


Figure 3.8 MTT cell viability of MC3T3-E1 cells in growth media cultured directly on MAO coated LAZ631. N=4, significance determined to be  $p < 0.05$ .

### 3.4 Discussion

MAO has been widely studied as a method to produce a corrosion and wear resistant coating on Mg and various alloys of Mg, but MAO itself is a very complex technique involving many different parameters that can greatly affect the corrosion resistance, coating morphology, as well as coating stability. These parameters include applied voltage and current, treatment time, electrolyte components and composition, as well as the alloying elements present within the Mg alloy. In this study, the operating parameters, treatment time, and electrolyte solution were utilized following prior research work and only the effect of alloying elements was studied [28]. In this research therefore, two alloy systems, LAZ and LZ, were used to study the effect of Li and Al content on the developed MAO coating in an alkaline phosphate, silicate, and fluoride containing

MAO electrolyte solution. The influence of Zn was not observed in the different alloys studied. This may be due to the addition of only 1wt. % of Zn. The effect of Li and Al on the characteristics, corrosion resistance and stability, as well as cytocompatibility of the MAO coating on the various Mg alloys was studied.

During MAO treatment of Mg and Mg alloys, both crystalline as well as amorphous phases are produced, with crystalline MgO being the most predominant phase. The coating is comprised of three distinct layers consisting of a thin transitional barrier layer between the metal and coating, a dense intermediate layer, and a porous outer layer [23]. Though MgO is the most predominant phase present within the coating, other phases can be introduced to increase the corrosion resistance through chemical and thermal reactions with the anions present in the electrolyte. These additional phases can include magnesium phosphates, silicates, and fluorides [23, 31]. Prior literature has reported that electrolytes containing KF increased the overall coating compactness via the presence of  $\text{MgF}_2$  within the coating, high amounts of Na lead to an overall decrease in pore size, and the presence of silicates and phosphates enabled the formation of  $\text{Mg}_2\text{SiO}_4$  and  $\text{Mg}_3(\text{PO})_4$ . [31]. The increased stability of these additional phases as compared to MgO leads to an increase in the corrosion resistance. Additionally, the MAO coating could indicate various compounds and phases containing the alloying elements.

The electrolyte solution used herein consisted of  $8 \text{ g L}^{-1} \text{Na}_2\text{SiO}_3$ ,  $6 \text{ g L}^{-1} \text{Na}_3\text{PO}_4$ , and  $4 \text{ g L}^{-1} \text{KF}$ . Due to the chosen electrolyte composition and prior literature we expected to see the presence of these silicates, phosphates, and fluorides within the MAO coatings [31]. XRD results (**Figure 3.2**) show characteristic peaks of MgO and  $\text{Mg}_2\text{SiO}_4$  phases within the MAO coatings on the LZ alloys and MgO,  $\text{Mg}_2\text{SiO}_4$ ,  $\text{LiAlSi}_4\text{O}_{10}$ , and  $\text{AlPO}_4$  within MAO coatings on the LAZ alloys. However, no characteristic peaks of any fluoride phases were detected. Further elemental analysis

of the surface of the MAO coatings revealed a small amount of F was detected only on LZ61 (0.19 wt. %) and LAZ631 (0.05 wt. %). Prior work has shown that MAO coated Mg-8.5Li-1Al within an electrolyte containing 10g/L  $K_2TiF_6$  contains  $MgF_2$  characteristic XRD peaks. Additionally, EDX elemental analysis of the cross section reveals that the majority of the presence of F was detected within the inner dense layer of the coating [32]. Additional MAO coating work on AZ31 in a fluoride-based electrolyte revealed that at low concentrations of F ( 0.05 M to 0.20 M),  $MgF_2$  characteristic peaks were not detected in XRD [33]. Between these two published studies, it can be construed that the concentration of F needed within the electrolyte solution to observe the presence of  $MgF_2$  is nearly 4-fold the amount used within the present study and thus is possibly the reason why we observed no  $MgF_2$  characteristic peaks. Further cross-sectional analysis needs to be conducted to examine the possible presence of F within the inner dense layer of the coatings.

Within the LZ alloys however, an increase of 3 wt. % Li leads to a decrease in Si content and an increase of O content on the surface of the coatings (**Figure 3.1 c and d**). These findings are supported by a decrease in  $Mg_2SiO_4$  and an increase in MgO characteristic peak intensities (**Figure 3.2 b and d**) with increasing Li content. Therefore it can be construed that an increase of Li content within the alloy leads to a more MgO rich coating. A similar trend for Li content is seen within the coatings on LAZ alloys as well. Investigation of the XRD spectra of the MAO coated LAZ alloys reveals the presence of  $AlPO_4$  and  $LiAlSi_4O_{10}$  characteristic peaks in addition to the MgO and  $Mg_2SiO_4$  phases. EDX shows similar results by revealing an increase of Si and P content on the MAO coated LAZ as compared to MAO coated LZ alloys (**Figure 3.1**).

The ability of the MAO coatings to increase the corrosion resistance of the various alloys was determined by both electrochemical corrosion tests as well as *in-vitro* immersion tests. The electrochemical corrosion tests gave insight into the corrosion resistance of the freshly prepared

MAO coated alloy, whereas the immersion tests provided knowledge of the degradation and stability of the coatings over time.

As described above, one of the factors important in determining the propensity of the corrosion resistance the MAO coating can provide is the phases present within the multi-layered ceramic coating. Within the two alloy systems studied, MgO and Mg<sub>2</sub>SiO<sub>4</sub> are present in both systems whereas AlPO<sub>4</sub> and LiAlSi<sub>4</sub>O<sub>10</sub> are only present in the LAZ alloy systems. The addition of these extra phosphate and silicate phases within the MAO coating have been shown to provide additional corrosion resistance to the Mg based alloys. Furthermore, the presence of Al during MAO has been shown to decrease the porosity and pore size (**Figure 3.1 a and b**) [23, 34, 35]. Therefore, Al results in a significant decrease in CR<sub>corr</sub> as compared to non-Al containing alloys due to the two above mentioned factors (**Table 3.1**). However, Li content did not significantly alter CR<sub>corr</sub> within the LAZ and LZ during PDP tests. Lastly, the CR<sub>corr</sub> of each of the MAO coated samples was significantly less than the bare alloys ( $p < 0.05$ ) (**Table 3.1**) indicating the positive influence of the MAO coatings on increasing the corrosion resistance of the Mg alloys.

Static in-vitro immersion degradation tests were performed for 5 weeks within HBSS at 37°C. After 1 week of immersion in HBSS, the Mg, Li, and Al concentration as well as pH of the collected immersion solution showed no difference between the MAO coated LAZ631, LAZ931, and LZ61 but MAO coated LZ showed an increase in the Mg ion release (**Figure 3.4**). After 3 weeks of immersion, LAZ931 showed increase in the Li ion release and LZ91 shows increase in Mg and Li ion release as well as the pH when compared to LZ61 and LAZ631. The same trend continues after 5 weeks of immersion. We believe that the decreased stability of the LZ91 and LAZ931 during immersion testing is due to the increased Li content in the alloys. Despite not being detected through XRD, it is possible that undetectable lithium rich phases were produced

and dispersed throughout the MAO process and included within the coating. Due to the higher solubility of lithium-based compounds (phosphates, fluorides, silicates), we hypothesize that the lithium-based phases formed begin to degrade at an increased rate as compared to the Mg, Al, and Zn based phases. Therefore, this process of soluble phases forming allows the surrounding solution to penetrate the coating and cause an increase in the corrosion at earlier time points. Additionally, when comparing between MAO coated LZ91 and LAZ931, the Mg and Li ion release data at 3 and 5 weeks reveals that the addition of Al partially counteracts the increased degradation caused by Li. We believe that this is due to the formation of the more stable  $\text{AlPO}_4$  and  $\text{LiAlSi}_4\text{O}_{10}$  phases produced in the presence of Al as seen in the diffraction patterns (**Figure 3.2**). In conclusion, we believe that the addition of Al counteracts the decreased coating stability caused by Li content. However, at increased amounts of Li content within the alloy, Al is no longer able to stabilize the coating resulting in an increased corrosion rate and dissolution of ions.

*In vitro* experiments, though not always completely representative, can aid in estimating the overall cytocompatibility of biomaterials when tested *in vivo*. In terms of Mg and Mg alloys, the large burst release of ions and hydrogen evolution associated with the rapid corrosion of the alloy when tested in-vitro often requires the use of in-direct testing methods. In the prior work of the Kumta group on LZ and LAZ alloys, such indirect methods of cell culture were used due to Mg ion concentrations reaching 2000 ppm for both systems within the extract medium after 3 days of immersion [1, 27]. The same extract had Li ion concentrations of 500 ppm for LZ alloys and up to 400 PPM for LAZ alloy [27]. Cell viability results revealed that a 10 fold dilution of the extracts allowed for the Mg and Li ions to play a beneficial on cell viability. However, the work herein has shown that the MAO coatings on the LAZ and LZ alloys were able to significantly reduce the Mg and Li ion release in HBSS (**Figure 3.4**). At the earliest time point of 1 week, the

Mg ion concentration for each coated alloy was around 20 ppm and the Li ion concentration ranged from 1 to 3 ppm, yielding a reduction in ion concentration of up to 100 fold as compared to the bare alloys after 3 days of immersion. Similarly, after 5 weeks of immersion, even our least corrosion resistant MAO coatings on LZ91 never allowed for Mg ion concentrations to reach higher than 80 ppm and Li ion concentrations higher than 30 ppm. Thus, we believed that our MAO coatings would be suitable to facilitate direct cellular attachment and proliferation. However, as seen from Live/dead staining images in **Figure 3.6**, live MC3T3 preosteoblast cells were only detected on MAO coated LAZ631 after 1 day of direct cell culture. The MTT results (**Figure 3.8**) further revealed that after 4 and 7 days of direct culture on MAO coated LAZ631, the metabolic activity of the pre-osteoblast cells significantly decreased from day 1 of culture revealing a decrease in the cellular viability. We hypothesize that despite this coating exhibiting the highest corrosion resistance as determined by PDP and immersion testing, the porous nature of the MAO coating still allows the solution to interact with the bare alloy allowing for corrosion to occur resulting in the formation of hydrogen gas (**Figure 3.7 b**) and thus having a negative effect on cytocompatibility. Similar results have been reported on observation of low cellular attachment and proliferation on cells seeded directly on MAO coated Mg alloys [28, 36].

Though these results are contradictory to our group's prior results obtained on indirect cell culture of the bare alloys, the results are explainable [28]. Indirect cell culture involving use of the extraction media only examines the response of the cells to the chemical cues arising from the ions and pH of the solution. However, cells directly cultured onto a biomaterial are affected by not only the ions and pH of the solution, but also by the material itself. The factors involved include surface morphology and pore size, surface roughness, material degradation and corrosion, as well as chemical cues directly contributing from the surface of the coating. Therefore, to fully



understand the complicated interaction of the cells with the MAO coated alloys further testing is required. Such tests involve conducting indirect cytocompatibility tests on the MAO coated samples [36, 37] to further evaluate only the effect of released ions and pH, as well as conducting further materials characterization analysis of the MAO coating and surface [26, 38, 39].

In the present work, MAO was utilized to create a corrosion resistant coating on high strength and ultra-high ductility (UHD) LZ and LAZ magnesium alloys to facilitate a decrease in ion release and an increase the material cytompatibility as compared to the bare alloys. Results indicated that the presence of Al within the alloys, allows for the generation of more stable additional phases throughout the MAO coating. These additional phases lead to an overall increase in the corrosion resistance as determined by electrochemical and immersion corrosion testing. Increased Li content however, within the alloy negatively influenced the stability of the MAO coating formed and facilitated faster degradation when immersed in HBSS. However, amongst all the MAO coated alloys, the MAO coating produced on LAZ631 exhibited the highest corrosion resistance during both corrosion tests and was the only coating able to exhibit signs of cytocompatibility with directly treated MC3T3 preosteoblast cells.

### **3.5 Conclusions**

In the present work, MAO was utilized to create a corrosion resistant coating on high strength and ultra-high ductility (UHD) LZ and LAZ magnesium alloys to facilitate a decrease in ion release and an increase material cytompatibility as compared to the bare alloys. Results indicated that the presence of Al within the alloys, allows for the generation of more stable additional phases throughout the MAO coating. These additional phases lead to an overall increase

in the corrosion resistance as determined by electrochemical and immersion corrosion testing. Increase in Li content within the alloy however, negatively influenced the stability of the MAO coating formed and facilitated faster degradation when immersed in HBSS. However, all MAO coated alloys displayed lower corrosion rates compared to the bare alloys. The MAO coating produced on LAZ631 possessed the highest corrosion resistance during both corrosion tests and was the only coating able to facilitate the attachment and proliferation of MC3T3 preosteoblast cells cultured directly onto the MAO coated alloy.

## **4.0 Resorbable Strontium Substituted Amorphous Calcium Phosphate and Dicalcium Phosphate Dihydrate Based Hydroxyapatite Forming Bone Cement**

### **4.1 Introduction**

Hydroxyapatite (HAp) bone forming cements as discussed in the introduction section are highly stable in physiological environments, possess low resorption rates in-vivo, and require longer setting times[15, 40]. In order to address these issues and counteract the limitations of HAp cements, amorphous calcium phosphate (ACP) has been incorporated within the precursor powders of numerous HAp forming cements [18, 41-43]. The lack of long-range atomic order and high specific surface area of ACP cements results in greatly increased solubility of the ACP cements and has shown to decrease the cement setting time [41]. In addition, ACP based HAp cements have been shown to fully resorb within 26 weeks in-vivo due to increased cement porosity and the formation of nano sized HAp crystals [44, 45]. However, the addition of ACP within the cement precursors does not come without introducing drawbacks. Incorporation of ACP within two different cement systems,  $\alpha$ -TCP and TTCP/MCPM based cements, results in a significant decrease of compressive strength as well as decreased in-vitro cell viability of the directly seeded MC3T3-E1 preosteoblasts due to conformational changes of the adsorbed proteins and rapid acidification of the media [18, 41].

Recently, the addition of strontium (Sr) within the HAp cementing system has been investigated due to the capability of Sr ions to stimulate the differentiation of osteoblast progenitor cells and limit osteoclastic resorption by interaction with the osteoblast and osteoclast paracrine signaling pathway[18, 46]. These studies have verified that Sr enriched HAp cements do in fact

result in increased cell proliferation as well as contribute to osteogenic differentiation in-vitro [18]. Additional studies on the effect of Sr on the mechanical properties of HAp cements have revealed an increase in compressive strength due to the formation of smaller HAp whiskers within SrHAp cements [18]. Furthermore, the addition of 10 mole% Sr within an ACP based HAp forming cement resulted in a 3-fold increase in compressive strength when compared to non Sr containing cements [42].

Here in the present study, the effect of Sr addition on an ACP and dicalcium phosphate dihydrate (DCPD) HAp forming cement system is reported. A second element of Sr was incorporated within the cement via substitution of Ca within the DCPD precursor as previously reported by our group [47]. Prior work on ACP/DCPD cement systems revealed that the formation of HAp is caused by hydrolysis of the separate precursors. Due to the high reactivity and solubility of ACP, the hydrolysis reaction to form HAp occurs very rapidly. Whereas due to the lower solubility of DCPD, the hydrolysis of DCPD will occur over a much longer period of time. Therefore, we hypothesized that the dual hydrolysis reaction of ACP and SrDCPD will facilitate the controlled formation of Sr substituted HAp resulting in controlled release of Sr ions. The influence of varying amounts of Sr content within the cement scaffolds on the cementing reaction, phase composition, cement porosity and specific surface area (SSA), and compressive strength was assessed. Furthermore, the effect of Sr content within the cement scaffolds on in-vitro proliferation and viability of MC3T3-E1 preosteoblasts was studied. To the best of our knowledge, the development and characterization of an ACP/SrDCPD cementing system has not been studied thus far. This work herein will provide fruitful knowledge and enable further understanding of Sr substitution within the CaP based cements.

## **4.2 Materials and Methods**

### **4.2.1 ACP precipitation**

All the reagents used for the synthesis were acquired from Sigma-Aldrich, USA and used in the form in which they were received. The synthesis of ACP was performed using a method previously described [48]. Solution A was made by adding of 11.0365 g of  $\text{CaCl}_2 \cdot \text{H}_2\text{O}$  and 5.0 g of  $\beta$ -cyclodextrin to 250mL of DI water. Solution B was made by adding 7.098 g of  $\text{Na}_2\text{HPO}_4$  into 250 mL of DI water. Both solutions were stirred at room temperature for 12 hours. Prior to mixing, the solutions were stirred at 4°C until the temperature of the solutions reached 15°C. The pH of solution A was then adjusted to 10 by dropwise addition of 1M NaOH solution. While constantly mixing, solution A was added dropwise to solution B while maintaining a pH of 10. The final solution was then stored at 4°C for 30 minutes. The precipitate was then collected by centrifuging the solution at 10,000 RPM for 5 minutes at 4°C. In order to remove any impurities, the collected precipitate underwent four separate washing and centrifuging steps consisting of two DI washes, a 50:50 water: acetone, and lastly only acetone. After washing, the precipitate was allowed to dry at room temperature. Finally, the precipitate was heated to 400°C for 2hours. Following heat treatment, the powders were stored in a desiccator until further characterization and use.

### **4.2.2 DCPD and strontium substituted DCPD precipitation**

All the reagents used for the synthesis were acquired from Sigma-Aldrich and used in the form in which they were received without any further purification. The synthesis of pure and

substituted DCPD was performed using a method previously described [47, 49].  $\text{CaCl}_2 \cdot 2\text{H}_2\text{O}$  and  $\text{SrCl}_2 \cdot 6\text{H}_2\text{O}$  powders following the stoichiometric ratio shown in **Table 4.1** were added to 100mL of DI water (**Table 4.1**). The  $\text{CaCl}_2 \cdot \text{H}_2\text{O}$  and  $\text{SrCl}_2 \cdot 6\text{H}_2\text{O}$  solution was added dropwise to the 0.5M  $\text{Na}_2\text{HPO}_4$  solution while constantly stirring at room temperature for 30 minutes. The precipitate was then centrifuged and washed with DI water. The final washing step was conducted in ethanol and the precipitate was dried at room temperature and then stored in a desiccator until further characterization and use.

**Table 4.1** The amount (mol) of the Ca and Sr containing precursors.

	$\text{CaCl}_2 \cdot 2\text{H}_2\text{O}$	$\text{SrCl}_2 \cdot 6\text{H}_2\text{O}$
Undoped	0.05	-
5% Sr	0.0475	0.0025
10% Sr	0.045	0.005
15% Sr	0.0425	0.0075

#### 4.2.3 Powder characterization

The phase composition of the powders formed was determined using X-ray diffraction (X-Pert PRO Cu  $K\alpha$   $\lambda=1.5418\text{\AA}$ , with X'celerator detector, Philips). During measurements, the X-ray generator was operated at 45 kV and 40 mA and the data was collected between  $2\theta$  values of  $10-90^\circ$ . Scanning electron microscopy (SEM, SEM; JSM6610LV, JEOL) was used to analyze the particle size and microstructure of the synthesized powders. The samples were sputter coated (Cressington, 108) prior to imaging.

#### 4.2.4 Cement characterization

Powder mixtures consisting of 75wt% ACP and 25wt% DCPD were prepared by hand mixing with a mortar and pestle. The cements were formed by adding 2%  $\text{Na}_2\text{HPO}_4$  solution with a powder to liquid ratio as seen in **Table 4.2**. Cements containing  $\text{Sr}^{2+}$  substitution of 0, 5, 10, 15 mole % within the DCPD are referred to as 0SrHA, 5SrHA, 10SrHA, and 15SrHA, respectively. The volume of liquid used for each composition was the least amount needed to produce a workable paste. To test the initial and final set times of each cement composition, a Gillmore Needle Apparatus was used. After complete setting, the cements were immersed in phosphate buffered saline (PBS) and incubated at 37°C for up to two weeks. At various time points during incubation, the cements were collected and the phase composition was analyzed using XRD.

**Table 4.2** Powder to liquid ratio used for each cement composition

Cement	Powder (g)	Liquid ( $\mu\text{L}$ )
0SrHA	1	1000
5SrHA	1	1050
10SrHA	1	1100
15SrHA	1	1150

The specific surface area of the cements prior and post incubation was measured from  $\text{N}_2$  adsorption-desorption isotherms using the Brunauer-Emmett-Teller method (Micrometrics ASAP 2020). The wet compressive strength of the cements scaffolds was analyzed using a 1kN load cell (Instron, Norwood, MA) with a crosshead speed of 1.3mm/min. SEM images were collected on the fractured surfaces post compression testing. A total of 6 cylindrical samples with a diameter

of 6mm and height of 12mm were analyzed for each condition. The % porosity of the cement scaffolds prior and post incubation in PBS was determined by using the following equation:

$$\%porosity = 1 - \frac{\rho_a}{\rho_T} \quad (4-1)$$

The true density  $\rho_T$  was determined using helium pycnometry (AccuPyc II 1340, Micromeritics, Norcross, GA) and the apparent density  $\rho_a$  was determined manually by dividing the mass of each sample by the volume. The volume of each sample in turn was also determined by manual calculation using the measured diameter and height of each sample.

#### **4.2.5 Mouse preosteoblast MC3T3-E1 cell culture**

MC3T3-E1 murine preosteoclast cell line was obtained from ATCC (Manassas, VA). Cells were cultured at 37°C in 5% CO<sub>2</sub> and 95% relative humidity in growth media containing minimum essential medium alpha (MEM $\alpha$ , Gibco, Grand Island, NY) which contained 10% fetal bovine serum (FBS, Atlanta Biologicals, Lawrenceville, GA) and 1% penicillin streptomycin (P/S, Gibco, Grand Island, NY). Prior to cell culture, all the samples were aged in PBS for 7 days and then sterilized using ethanol and ultraviolet light. The cells were directly seeded onto the cement scaffolds at a density of 50,000 cells per well. Growth media was changed daily.

#### **4.2.6 Live/dead staining**

The attachment and proliferation of MC3T3-E1 cells seeded directly on the cement scaffolds was assessed by live/dead staining (Invitrogen, Live/Dead staining kit) after day 1 and



day 3 of cell culture in the growth media comprising minimum essential medium alpha (MEM $\alpha$ , Gibco, Grand Island, NY) which contained 10% fetal bovine serum (FBS, Atlanta Biologicals, Lawrenceville, GA) and 1% penicillin streptomycin (P/S, Gibco, Grand Island, NY). At day 1 and day 3 of culture the samples were rinsed twice with PBS and incubated in PBS containing the live/dead stain for 30 minutes. The PBS containing the live/dead stain was removed and replaced with fresh PBS. Imaging was conducted using an Olympus CKX41 fluorescent microscope.

#### **4.2.7 Direct MTT assay**

Cell viability of cells directly seeded on the cement samples was assessed using the MTT activity assay (Vybrant MTT Cell Proliferation Assay Kit). The cells were subjected to 500  $\mu$ L of fresh growth media comprising minimum essential medium alpha (MEM $\alpha$ , Gibco, Grand Island, NY) which contained 10% fetal bovine serum (FBS, Atlanta Biologicals, Lawrenceville, GA) and 1% penicillin streptomycin (P/S, Gibco, Grand Island, NY) and 50  $\mu$ L of 12mM (3-(4,5-Dimethylthiazol-2-yl)-2,5-diphenyltetrazolium bromide) solution and incubated for 4 hours. After incubation, 500  $\mu$ L of sodium dodecyl sulphate was added and incubated for 18 hours to solubilize the formazan. After 18 hours, 200  $\mu$ L of each sample's solution was transferred to a 96 well plate and the absorbance of the sample was measured using Synergy2 Multi-Mode Microplate Reader (Biotek, USA) with an emission wavelength of 570nm.

#### **4.2.8 In-vitro dissolution test**

In order to evaluate the pH and ion concentration of the environment the cells encounter during in-vitro cytocompatibility tests, cement samples were immersed in growth media

comprising minimum essential medium alpha (MEM $\alpha$ , Gibco, Grand Island, NY) which contained 10% fetal bovine serum (FBS, Atlanta Biologicals, Lawrenceville, GA) and 1% penicillin streptomycin (P/S, Gibco, Grand Island, NY) and stored at 37°C and 95% relative humidity for three weeks. The media was changed daily and at various time points the pH of the media was measured and collected for analysis of ion concentration. Mg, Sr, and PO<sub>4</sub> concentration was measured by inductively coupled plasma-optical emission spectroscopy (ICP-OES, iCAP duo 6500 Thermo Fisher). 1mL of the collected media was diluted 10 fold by adding 9mL of 3% HNO<sub>3</sub> in DI water. A standard calibration curve was generated by using known amounts of Mg and Sr elemental standards diluted in 3% HNO<sub>3</sub> to the desired concentration range. The standard calibration curve was used to evaluate the concentration of each ion in the solution.

#### **4.2.9 Statistical Analysis**

A one-way analysis of variance (ANOVA) was used to determine the statistical significance defined by  $p < 0.05$ . The Tukey post-hoc test was used to determine the statistical significance between the different conditions.

### **4.3 Results**

#### **4.3.1 Powder characterization**

The cementing reaction is highly dependent on the crystallinity, phase composition, and particle size of the precursor powders. Thus, XRD was used to evaluate the phase composition

and crystallinity of the synthesized ACP, Sr doped DCPD, and undoped DCPD powders (**Figure 4.1**). As seen in the prior work conducted on the aqueous synthesis of Sr doped and undoped DCPD, the only phase present is DCPD. The higher relative intensity of the peak at  $12^\circ$  corresponds to the preferred orientation along the (020) direction [47]. The XRD pattern of the prepared ACP powder reveals a very broad pattern with no detection of characteristic crystalline peaks. This pattern is indicative of an amorphous material and thus confirms the formation of amorphous calcium phosphate (ACP). Further analysis of the particle size of the synthesized powders was performed by SEM (**Figure 4.2**). **Figure 4.2 (a-b)** reveals a typical broad plate like morphology for the undoped and Sr doped DCPD powders characteristic of the brushite phase. The undoped DCPD powder consists of particles that are approximately  $15\text{ }\mu\text{m}$  in width and varying in length. Addition of 15%Sr results in an overall decrease in particle size. Prior work has also concluded that a decrease in DCPD particle size ( $\sim 5\text{ }\mu\text{m}$ ) was observed when doped with 10% Sr whereas doping with 5% Sr did not change the particle size [47]. The images of the synthesized ACP powders as shown in **Figure 4.2 (c-d)** reveals agglomerates of nano sized amorphous particles with spherical morphology.

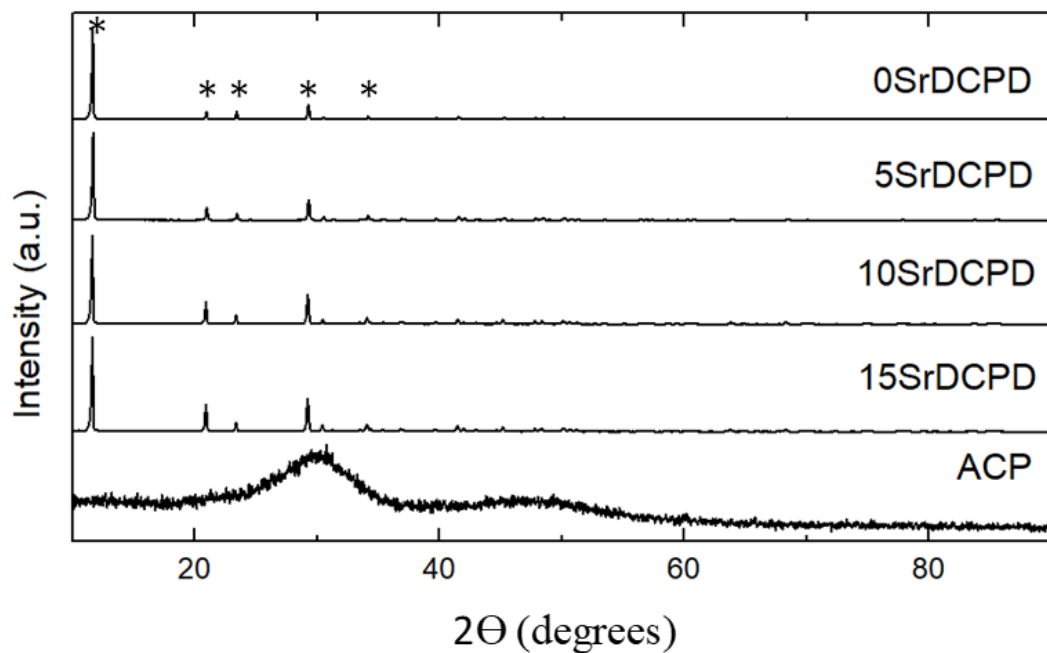


Figure 4.1 X-ray diffraction pattern of synthesized precursor powders. \* denotes DCPD characteristic peaks (JCPDS 09-0077).

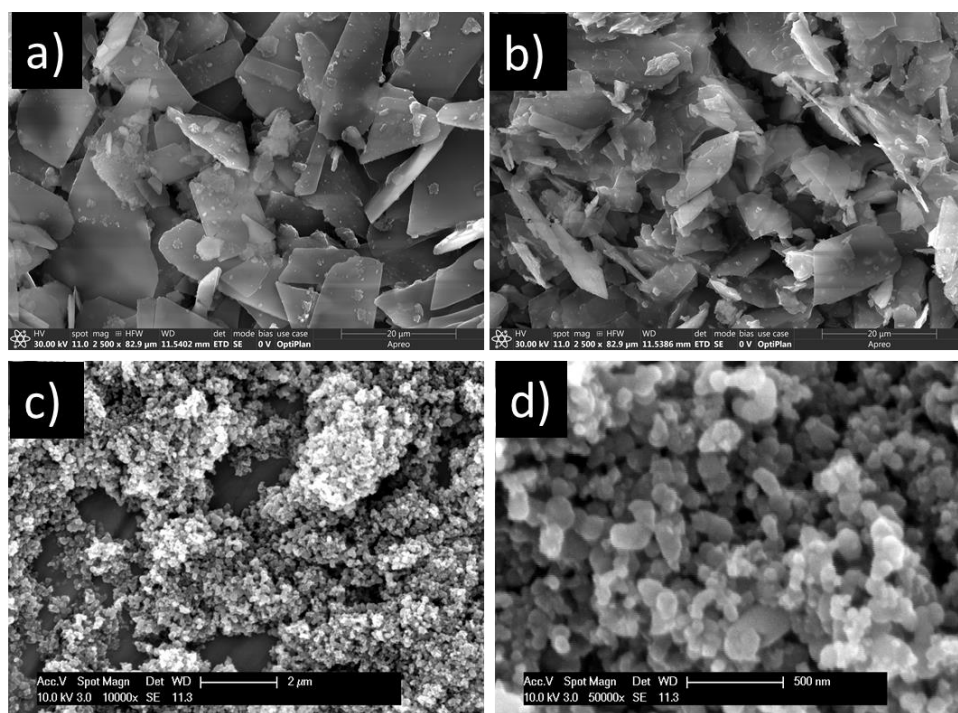


Figure 4.2 SEM images of synthesized a) 0SrDCPD, b) 15SrDCPD, c-d) ACP.

## 4.3.2 Cement Characterization

### 4.3.2.1 Setting time

The setting time of the cementing reaction is a critical property of a cement if it is to be used in a clinical setting. Therefore, the setting time of each of the cements was measured at both room temperature and at 37°C under physiological conditions (**Figure 4.3**). At room temperature, 0SrHA displayed the shortest initial ( $14 \pm 1.2$  minutes) and final ( $24 \pm 0.80$  minutes) setting times whereas 15SrHA had the longest initial ( $20 \pm 2.1$ min.) and final ( $45 \pm 2.3$  min.) setting times. Setting at 37°C however, accelerates the reactions leading to an expected overall decrease in setting times, but despite the decrease in setting time, the same trend of Sr content increasing the setting times was nevertheless, seen. Therefore, at 37°C 0SrHA had the shortest initial ( $6 \pm .9$  minutes) and final ( $14 \pm 2.2$ min.) setting times and 15SrHA had the longest initial ( $12 \pm 0.7$  min.) and final ( $30 \pm 1.8$  min.) setting times.

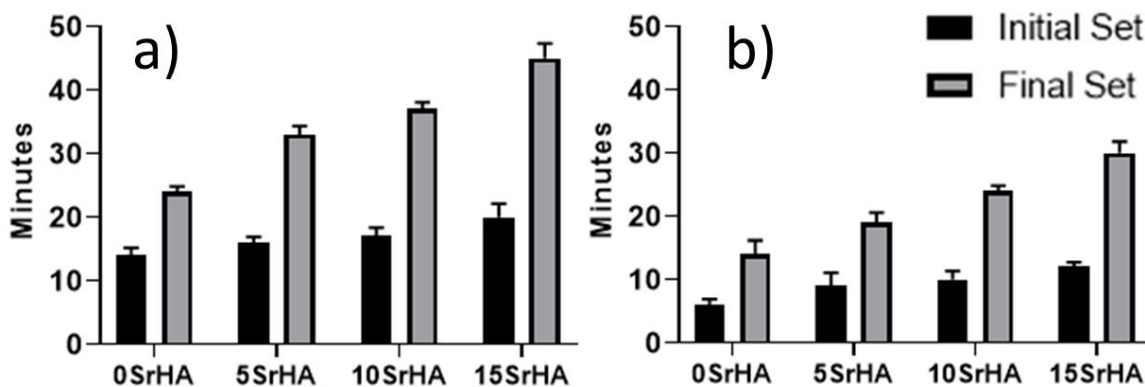
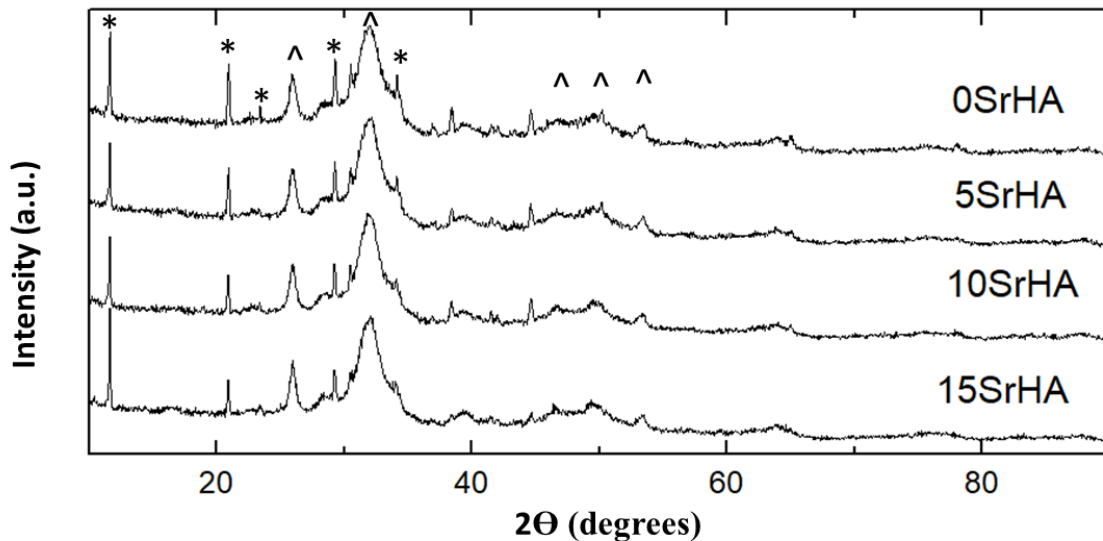


Figure 4.3 The average setting times of the cements prepared with a 75:25 ACP:DCPD ratio by weight at a) room temperature and b) 37°C. N=3.

#### 4.3.2.2 Phase Composition

In order to analyze the hydrolysis of the cement forming precursors ACP, DCPD, and SrDCPD powders and evaluate the formation of HAp, XRD of the cements was conducted following final setting and incubation in PBS for up to two weeks. **Figure 4.4** depicts the XRD pattern collected from the cements after the final setting time. XRD patterns revealed a biphasic composition consisting of poorly crystalline HAp and unreacted DCPD for all of the cements. The intensity of the DCPD peaks around  $21^\circ$  and  $29^\circ$  were reduced as the Sr content was increased within the cements suggesting a decrease in the amount of unreacted DCPD. After immersion in PBS for 14 days however, the XRD spectra of 0SrHA and 5SrHA cements revealed a biphasic composition of HAp and unreacted DCPD, however a reduction of DCPD peak intensities was identified (**Figure 4.5**). XRD pattern of 10SrHA and 15SrHA cements after 14 days immersion in PBS on the other hand revealed only poorly crystalline HAp formation. These results suggest increased solubility of DCPD with increasing Sr content, specifically for 10mole% and 15mole%.



**Figure 4.4** X-ray diffraction spectra of prepared undoped and doped cements after final setting. \* denotes DCPD characteristic peaks (JCPDS 09-0077). ^ designates HAp characteristic peaks (JCPDS 09-0432).

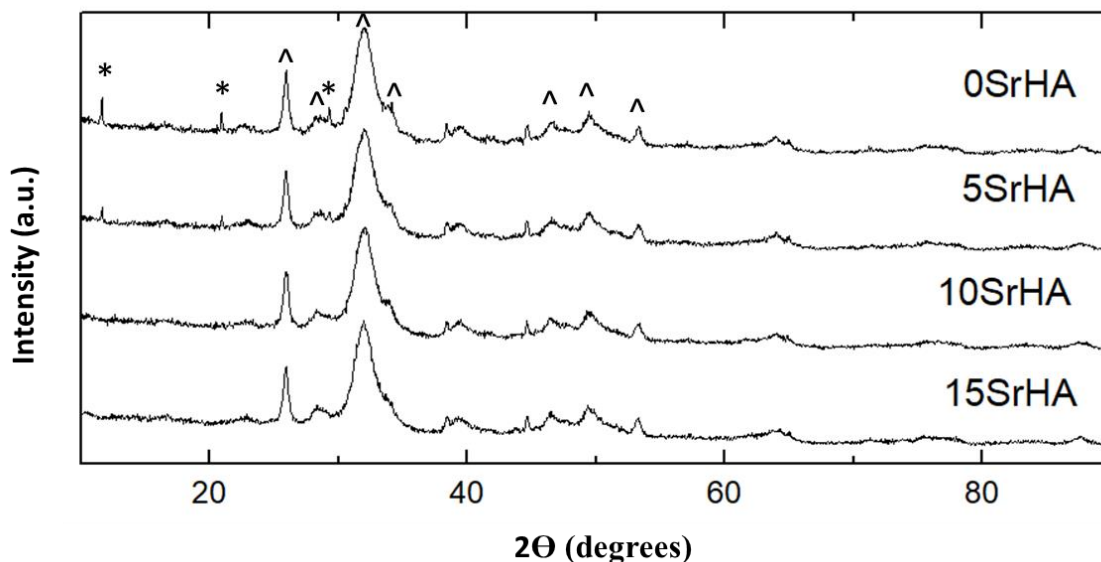


Figure 4.5 X-ray diffraction spectra of cements after 14 days immersion in PBS. \* denotes DCPD characteristic peaks (JCPDS 09-0077) . ^ designates HA characteristic peaks (JCPDS 09-0432).

#### 4.3.2.3 Wet compressive strength and % porosity

Even though no CaP cements are used for load bearing defects, the scaffolds still need to be able to withstand passive compressive forces. Therefore, the wet compressive strength was determined for the as-prepared scaffolds after immersion in PBS for up to 2 weeks (**Figure 4.6 a**). During the 2 weeks of immersion in PBS, the compressive strength of the scaffolds varied between approximately 1 to 3 MPa. After day 1, the compressive strength of 5SrHA ( $2.67 \pm 0.50$  MPa) was significantly higher than 15SrHA ( $1.79 \pm 0.17$ MPa) ( $p < 0.05$ ). At day 7, 5SrHA ( $2.31 \pm 0.27$  MPa) was significantly higher than 0SrHA ( $1.17 \pm 0.43$ MPa), 10SrHA ( $1.52 \pm 0.23$  MPa), and 15SrHA ( $0.98 \pm 0.03$  MPa) ( $p < 0.05$ ). A similar trend was seen at day 14.

The percent porosity of the cement scaffolds directly affects the compressive strength of the cement scaffolds and was thus calculated by measuring the true and apparent density at various time points after immersion in PBS for up to 2 weeks (**Figure 4.6 b**). The high porosity values

after immersion in PBS ranging from 60% to 70% indicate highly porous nature of the cements and explains the low wet compressive strengths as seen in **Figure 4.6a**. After 1-day immersion in PBS the highest % porosity (71.15%) and lowest (59.44%) between all the cements was measured in 0SrHA and 15SrHA, respectively. However, after 14 days immersion, 15SrHA shows the highest %porosity (69.5%) and 0SrHA shows the lowest (59.44). 10SrHA exhibits a similar trend as 15SrHA and exhibits increased %porosity after 14 days immersion in PBS. Whereas 5SrHA exhibits a similar trend as 0SrHA and exhibits decreased %porosity after 14 days immersion in PBS.

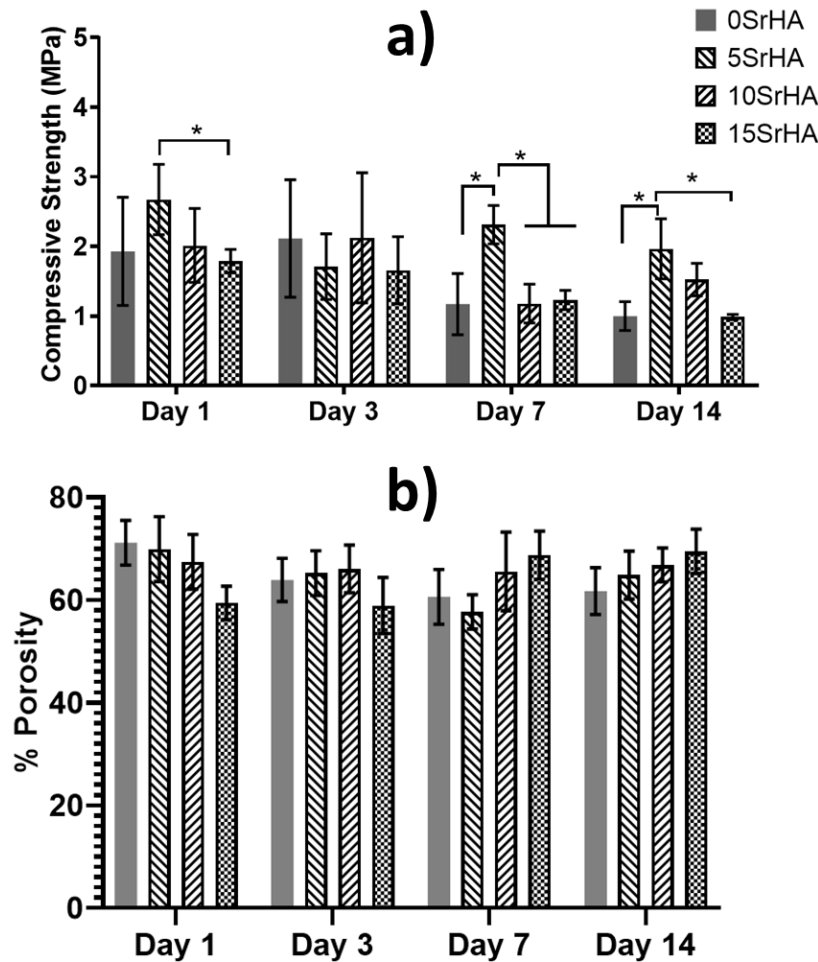


**Figure 4.6** Wet compressive strength (N=6) and b) % porosity of cement scaffolds after final setting and immersion in PBS (N=3). Significance was determined by  $p < 0.05$ .



In order to further investigate the highly porous property of the cements, SEM images of the fracture surface after compression testing were taken. Figure 4.7 (a, b) reveals the presence of the newly precipitated HAp as well as entrapped unreacted undoped and 5% substituted DCPD after final setting within the 0SrHA and 5SrHA cements, respectively, as indicated by the XRD diffraction patterns (Figure 4.4-4.5). The presence of pores approximately 20  $\mu\text{m}$  in diameter resulted from the highly inter-aggregate distance present due to the large amount of liquid needed for mixing. After 14 days immersion in PBS, SEM images of 0SrHA reveals the presence of unreacted DCPD, but also contains smaller rectangular pores formed from the dissolution of the DCPD particles (Figure 4.7c). The same rectangular pores were detected in 15SrDCPD after 14 days immersion in PBS, but no unreacted Sr substituted DCPD particles were detected. The absence of unreacted DCPD imaged in 15SrHA and presence of DCPD imaged in 0SrHA after 14 days immersion directly correlate with the XRD results (Figure 4.5). Furthermore, the increase of porosity of 15SrHA after 14 days can be attributed to the complete dissolution of the Sr substituted DCPD and lack of precipitation of newly formed HAp within its place. A similar decrease in porosity of 0SrHA would be expected after complete dissolution of DCPD particles following immersion in PBS even beyond the 14 days considered in this study.

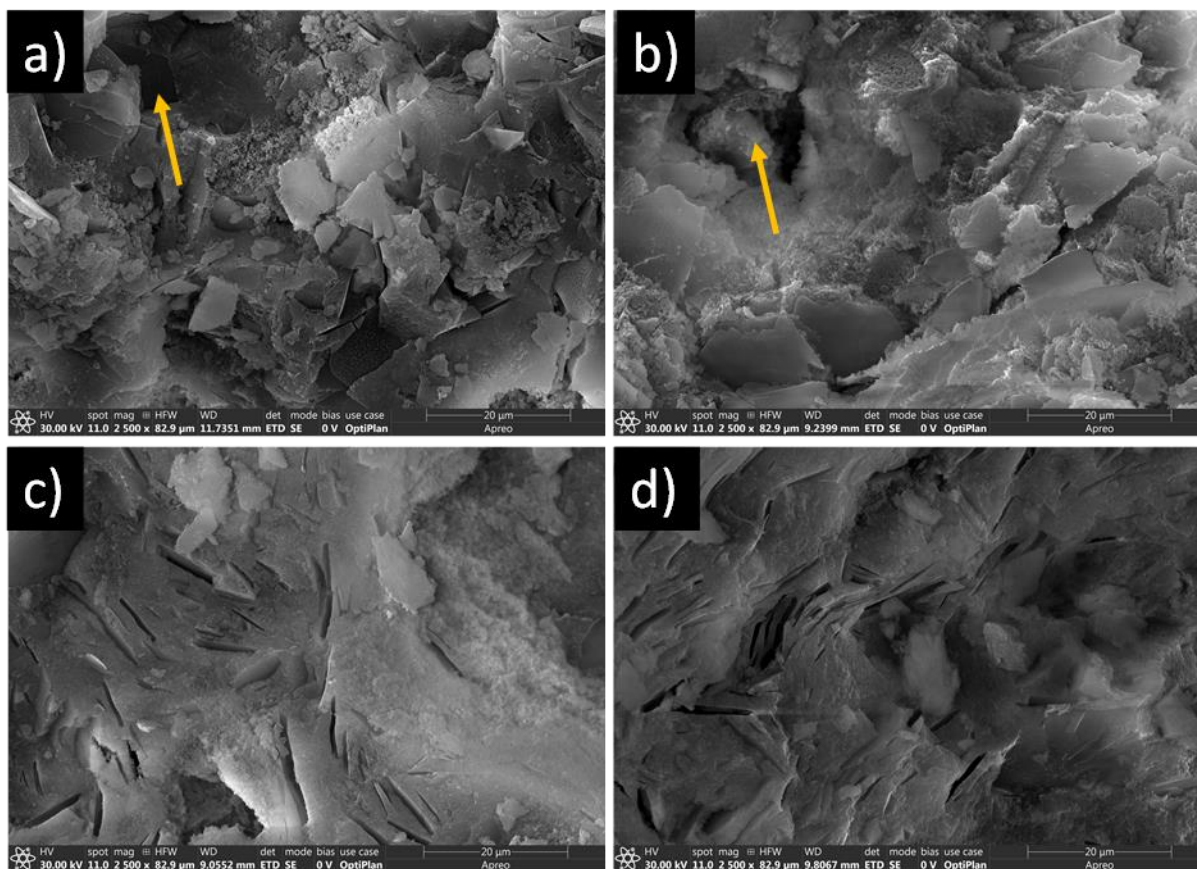


**Figure 4.7** SEM images of the fracture surface of a) 0SrHA, b) 15SrHA after final setting and c) 0SrHA, d) 15SrHA after 14 days immersion in PBS. Arrows indicate pores formed during cement mixing.

#### 4.3.2.4 Cement specific surface area

Evaluation of the formation of HAp was performed by analysis of the specific surface area of the cements. As seen in **Figure 4.8**, an increase of  $SSA_{BET}$  is observed in 15SrHA cements after 7 days immersion in PBS ( $95.58 \text{ m}^2/\text{g}$ ) as compared to after final setting ( $50.15 \text{ m}^2/\text{g}$ ) at day 0 and is due to the dissolution of the micron sized DCPD particles and precipitation of a nanosized HAp (NanoHAp) final phase. Further dissolution of the SrDCPD and formation of NanoHAPs in 5SrHA, 10SrHA, and 15SrHA allows for a significantly higher  $SSA_{BET}$  of 172.83, 165.98, and  $151.76 \text{ m}^2/\text{g}$ , respectively, as compared to 0SrHA ( $p < 0.05$ ).

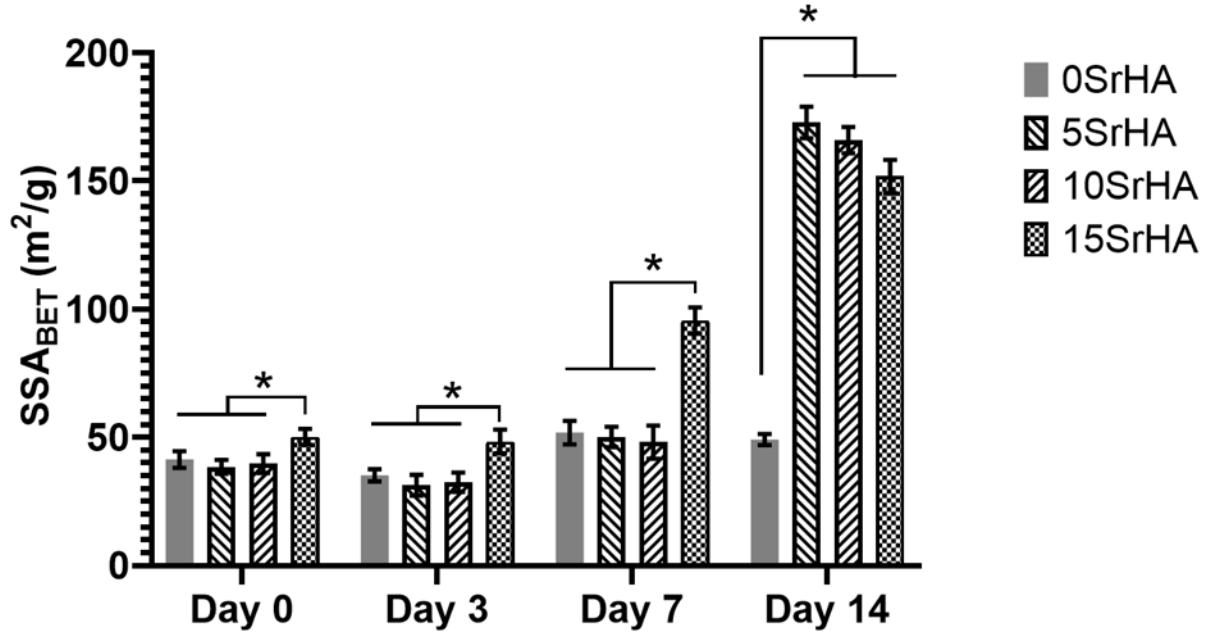
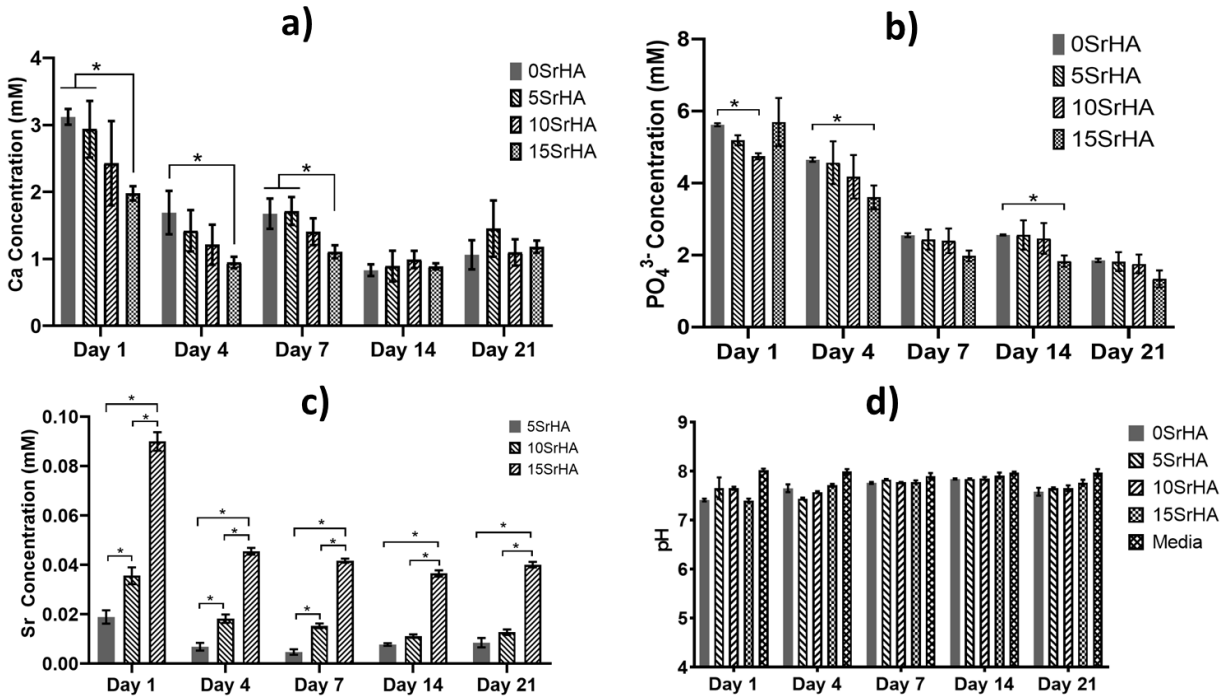


Figure 4.8 .  $SSA_{BET}$  measurements of cement scaffolds after final setting and 14 days of immersion in PBS. N=3

#### 4.3.3 In-vitro dissolution and cytocompatibility tests

In order to measure the ionic concentration and pH of the solution that cells would be cultured in, doped and undoped cements were immersed in 2mL of growth media comprising of minimum essential medium alpha (MEM $\alpha$ , Gibco, Grand Island, NY) which contained 10% fetal bovine serum (FBS, Atlanta Biologicals, Lawrenceville, GA) and 1% penicillin streptomycin (P/S, Gibco, Grand Island, NY) maintained at 37°C for up to 21 days and the  $Ca^{2+}$ ,  $Sr^{2+}$ , and  $PO_4^{3-}$  concentrations and pH were measured at various time points, while changing media daily (**Figure 4.9**). The basal concentrations of  $Ca^{2+}$  and  $PO_4^{3-}$  within the growth media were 1.8mM and 1.0mM respectively. **Figure 4.9 d** depicts slight acidification of the media at days 1 and 4 of immersion for all of the cements caused by dissolution of the DCPD. However, after 7 days immersion, the pH of all the cements were comparable to the media. After 1-day immersion in growth media

comprising minimum essential medium alpha (MEMα, Gibco, Grand Island, NY) which contained 10% fetal bovine serum (FBS, Atlanta Biologicals, Lawrenceville, GA) and 1% penicillin streptomycin (P/S, Gibco, Grand Island, NY) the  $\text{Ca}^{2+}$  concentration of the solutions collected from the cement samples were between 1.98 and 3.12 mM and were higher than the media (**Figure 4.9 a**). The increase in  $\text{Ca}^{2+}$  suggests rapid dissolution of the precursors. At day 4 of immersion, the  $\text{Ca}^{2+}$  concentration of all of the cement samples were below the basal level of the media and suggests the commencement of HAp formation on the surface of the cements. At 1, 4, and 7 days of immersion, the  $\text{Ca}^{2+}$  concentration of 15SrHA cements was significantly lower compared to 0SrHA ( $p < 0.05$ ). At days 14 and 21, the  $\text{Ca}^{2+}$  concentration for all the cements remained below basal levels of the growth media. Not unlike the  $\text{Ca}^{2+}$  concentration, the  $\text{PO}_4^{3-}$  concentration was highest at day 1 of immersion (4.74-5.69 mM) for all the cements and decreased over time. However, the  $\text{PO}_4^{3-}$  concentration was higher than the basal level at each time point further suggesting and validating the dissolution of unreacted DCPD (**Figure 4.9 b**). **Figure 4.9 c** depicts that after an initial burst release of  $\text{Sr}^{2+}$  ions at 1 day of immersion of Sr containing cements (0.02 to 0.9 mM), the  $\text{Sr}^{2+}$  concentration remains steady up to 21 days for all the Sr containing cements (0.008 to 0.045 mM).



**Figure 4.9** The concentrations of a)  $\text{Ca}^{2+}$ , b)  $\text{PO}_4^{3-}$ , c)  $\text{Sr}^{2+}$  as measured by ICP and d) pH of cements immersed in cell growth media maintained at 37°C.

Evaluation of the effect of Sr on the in-vitro cytocompatibility of the cement scaffolds was performed by direct seeding of MC3T3-E1 preosteoblasts on the cements. Live/Dead staining after day 1 of culture qualitatively reveals an increase in the density of live cells with increasing Sr content of the cement scaffolds (**Figure 4.10 a-d**). After 4 days of culture in growth media comprising minimum essential medium alpha (MEMα, Gibco, Grand Island, NY) which contained 10% fetal bovine serum (FBS, Atlanta Biologicals, Lawrenceville, GA) and 1% penicillin streptomycin (P/S, Gibco, Grand Island, NY), a similar trend is observed but the density of the cultured cells is increased, especially for cells cultured on 10SrHA and 15SrHA (**Figure 4.10 e-h**). The qualitative effect of Sr content was quantified by the MTT assay which matches with the Live/Dead assay (**Figure 4.11**). After 1 day, cells cultured on 10SrHA and 15SrHA displayed significantly higher cell viability as compared to 0SrHA and 5SrHA ( $p < 0.05$ ). After 4 days, an

increase in cell viability was observed amongst all groups as compared to day 1. However, the 10SrHA and 15SrHA cements showed significantly higher cell viability as compared to 0SrHA and 5SrHA cements ( $p<0.05$ ) showing the positive influence of Sr.

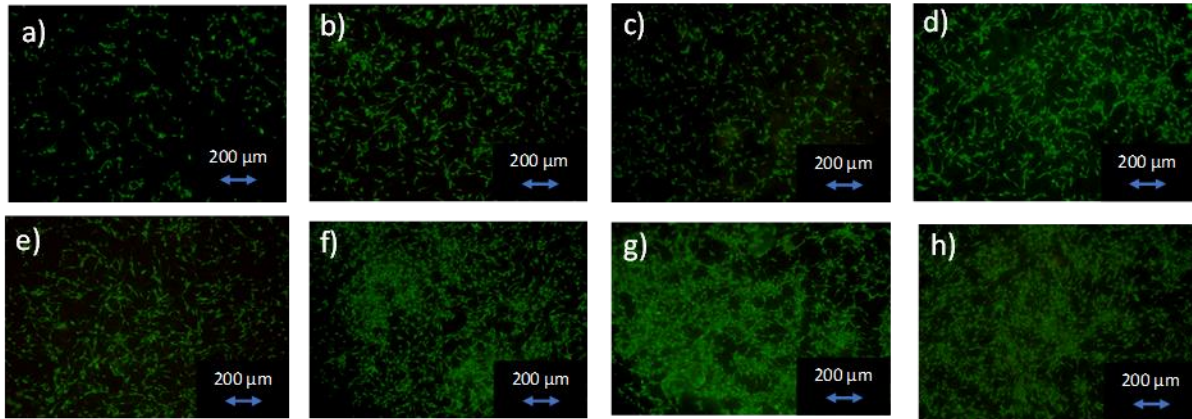


Figure 4.10 Live/Dead staining of MC3T3-E1 cells cultured in growth media on a) 0SrHA, b) 5SrHA, c) 10SrHA, d) 15SrHA after 1 day and e) 0SrHA, f) 5SrHA, g) 10SrHA, and h) 15SrHA after 4 days.

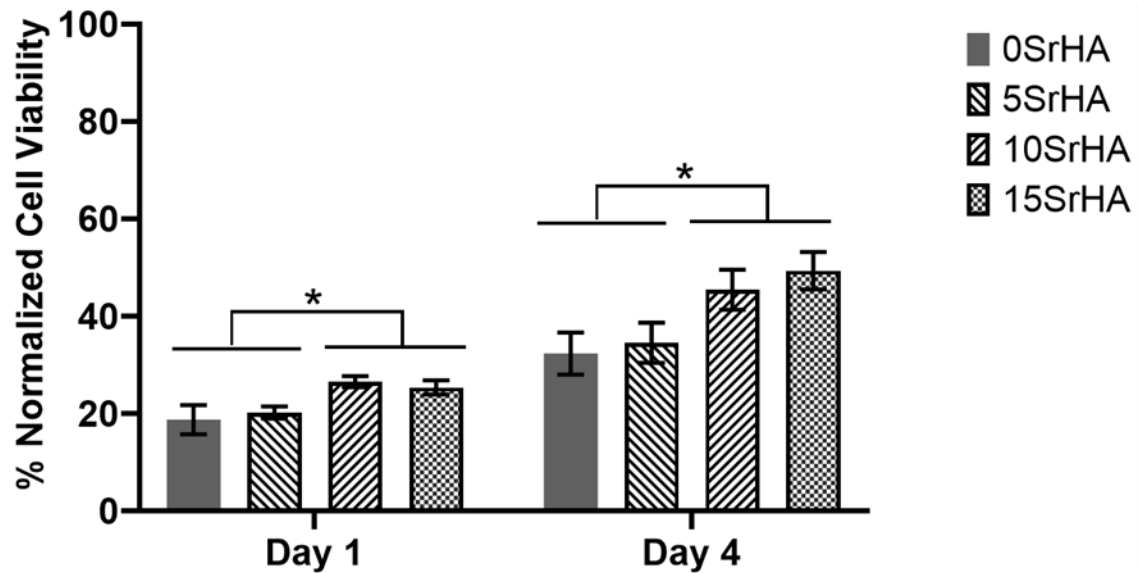


Figure 4.11 MTT cell viability of MC3T3-E1 cells in growth media cultured directly on cement samples. N=3.

## 4.4 Discussion

The conversion of the ACP and SrDCPD precursor powders to the final HAp phase in the cement following the completion of the cement setting reaction occurs by dual hydrolysis of both the precursor powders. Due to a lack of long-range atomic order and absence of nano sized crystalline particles, the ACP is highly reactive and solubilizes almost instantly when the liquid phase is added and creates a supersaturation of Ca and  $\text{PO}_4$  ions in the liquid phase. Simultaneously, some of the less soluble SrDCPD dissolves into the liquid and releases additional  $\text{Ca}^{2+}$  and  $\text{PO}_4^{3-}$  ions as well as  $\text{Sr}^{2+}$  ions. Once supersaturation of the ions in the liquid phase is attained, the HAp and SrHAp phased cement set due to precipitation of a HAp matrix that surrounds the unreacted DCPD powder. As seen in **Figure 4.3**, the setting time (initial and final) is prolonged with increasing Sr content in the DCPD and is due to the inhibitory effect Sr ions on the formation of the apatite phase [18, 42, 47]. After final setting time is reached, the cement consists of a biphasic composition consisting of unreacted DCPD or SrDCPD particles surrounded by a poorly crystalline HAp or SrHAp matrix (**Figure 4.4**). After immersion in PBS for 14 days, the XRD results reveal that 10SrHA and 15SrHA cements no longer contain any unreacted DCPD particles and the phase composition consists of only pure HAp phase. Increased solubility of the Sr substituted DCPD has been observed in prior work published from our group [47]. The increase in solubility is attributed to lattice expansion caused by the substitution of larger Sr ions within the DCPD crystal structure.

One of the main objectives of this work was to form Sr substituted HAp cements. Though the XRD patterns in **Figure 4.5** show the formation of a poorly crystalline HAp final phase, these patterns do not confirm the formation of Sr substituted HAp. However, examination of the Sr ion concentration induced by cement dissolution into the growth media (**Figure 4.9c**) along with the

XRD patterns in **Figure 4.5** confirms the formation of SrHAp. The release of ions within the growth media can occur by two different processes. The first method of Sr ion release is by the dissolution of the unreacted SrDCPD followed by the diffusion of Sr ions into the surrounding liquid that do not participate in the precipitation reaction. The second method is the infusion of  $\text{Sr}^{2+}$  ions by the direct dissolution of the newly formed HAp. If the HAp does in fact contain substituted Sr ions within the apatite lattice structure, then a continued release of  $\text{Sr}^{2+}$  ions should continue even after complete hydrolysis of SrDCPD, as seen in **Figure 4.9c** for 10SrHA and 15SrHA cements. Thus, the XRD patterns along with the ICP results confirm the formation of Sr substituted HAp. More studies however, need to be done.

It is well known within the literature that ACP based cements require a much higher amount of liquid during mixing in order to create a workable paste as compared to other less reactive hydrolysable precursors such as  $\alpha$ -TCP[15, 18, 42, 43] due to the large surface area (  $\sim 60 \text{ m}^2/\text{g}$ ) of ACP [43]. The large amount of required liquid phase increases the inter-aggregate distance between the newly precipitated HAp phase and results in a highly porous cement with low compressive strength as seen in **Figure 4.6 (a, b)** [41, 50]. The precipitation of NanoHAp increases porosity due to the formation of a large number of particles and micropores. Interestingly, despite the increased amount of liquid needed for higher mole % Sr substitution of DCPD there was no significant difference in porosity amongst all the cement samples. Further investigation of the compressive strengths of the cement scaffolds reveals that Sr content significantly increased compressive strength, especially 5SrHA cement after 7- and 14-days immersion in PBS. A similar effect of Sr within a biphasic HAp- $\text{SrCO}_3$  cement system was attributed to the formation and entanglement of nano sized SrHAp whiskers causing the increased compressive strength. However, it was also reported that at Sr contents higher than 10 mole %



within the cement a decrease in compressive strength was seen [20]. Therefore, it is possible that the Sr content of the 5SrHA cement is within the optimum range needed to increase the compressive strength of the cements.

In comparison to other ACP/DCPD based HAp forming cements, the compressive strength obtained herein (~1 MPa to 3 MPa) falls within the 0.7 MPa to 10 MPa range for similar cements [41, 50]. Additionally, it is known throughout in the literature that CaP cements are not intended for use in any load-bearing applications and thus high compressive strengths are not required. Instead the aim for all bone cement applications is the ability of the cement to maintain structural stability during the entire bone healing process. More importantly, it is critical that the cements following setting reaction remain structurally stable and not disintegrate when immersed in physiological body solutions particularly, blood. The stability of all the cements prepared in this study in PBS and growth media is indeed an indication of the structural integrity of the prepared cements in line with the compression strengths with published literature. All of the cements prepared within this study therefore exhibited the required structural stability when immersed in PBS for 2 weeks and growth media for 3 weeks and therefore expected to maintain structural integrity when used in-vivo.

Due to the formation of NanoHAp and the resultant high specific surface area of ACP based cements, it was originally believed these cements would facilitate increased in-vitro cellular attachment and proliferation because of the increased protein adsorption. However, studies have shown that the addition of ACP in HAp cements actually decreases cellular attachment and proliferation of MC3T3-E1 cells [41, 51]. The authors hypothesized this was due to a conformational change of the adsorbed proteins onto the surface of the cements, however no studies were done to confirm this hypothesis. However, the in-vitro cytocompatibility tests

conducted herein shows that a constant release of Sr ions from the SrHAp cement scaffolds causes increased MC3T3-E1 cell density as well as significantly increased viability when the concentration of Sr ions in the growth media is 0.015 to 0.042 mM (**Figure 4.10 - 4.11**). Singh et al. has also shown the increased cell viability of MC3T3 cells seeded directly on SrDCPD/TTCP based cement scaffolds when the concentration of Sr in the growth media is approximately 0.05 mM [47]. Additionally, Liu et al. reported that with human bone marrow stromal cells (hbMSCs) cultured directly on SrHAp cement scaffolds an increase in proliferation and osteogenic differentiation was observed for similar Sr concentrations in the culture media [52]. Our observations are therefore in line with the observations of other researchers reported in the literature.

As previously discussed, one of the advantages of ACP based HAp forming bone cements is their increased solubility and higher resorption rates as compared to other more traditional HAp cements. The increased solubility of ACP based cements has been attributed to the formation of a poorly crystalline NanoHAp cement matrix with high specific surface area. The SrHAp cements studied herein exhibit both a poorly crystalline SrHAp phase composition (**Figure 4.5**) as well as  $SSA_{BET}$  values ( $\sim 150\text{-}170\text{ m}^2/\text{g}$ ) indicative of nano sized particles (**Figure 4.8**) after 14 days immersion in PBS. Therefore, we believe that these ACP/SrDCPD cements will also exhibit increased solubility and resorption rates in-vivo. More studies are however, needed to be conducted to confirm this theory.

## 4.5 Conclusions

In the present work, highly porous Sr substituted NanoHAp forming cements were prepared by a dual hydrolysis reaction of ACP and SrDCPD cement precursors. The cements were capable of setting at room temperature and setting time linearly increased with increasing Sr content. Complete hydrolysis of all precursors into NanoSrHAp was accelerated by increasing the amounts of Sr content. All of the Sr containing cements facilitated a constant release of Sr ions when immersed in cell culture growth media for up to 3 weeks and maintained structural stability, albeit exhibiting low compressive strength similar to other ACP based cements. Cements prepared with 10 mole % and 15 mole % Sr substituted DCPD supported increased MC3T3-E1 proliferation and cell viability as compared to cements prepared with unsubstituted and 5 mole % Sr substituted DCPD. Further work however, needs to be conducted to understand the role of Sr on the solubility, dissolution rate and in-vitro cytocompatibility of the cements.

## 5.0 Summary and Future Work

In the work conducted herein, a biodegradable ACP/SrDCPD HAp forming cement and a biodegradable bioceramic coating on novel ultrahigh ductility (UHD) Li, Al and Zn containing LAZ and LZ Mg alloys were studied in detail. The effect of the soluble inorganic ions on the materials properties of the cement, the cement scaffold characteristics, corrosion and dissolution rate, and in-vitro cytocompatibility was analyzed.

In order to improve the materials and biological properties of the ACP/DCPD based cement, Sr ions were incorporated into the cement via substitution of the  $\text{Sr}^{2+}$  ions into the DCPD precursor. During the cementing reaction, both the precursors underwent hydrolysis and resulted in the formation of a NanoSrHAp cement, albeit at different rates in accordance with their different solubilities. Sr substituted DCPD particles exhibited increased solubility enabling a faster phase transformation to NanoSrHAp during aging in PBS. All of the SrHAp cements were able to constantly release  $\text{Sr}^{2+}$  ions while immersed in the growth media for up to 21 days. The released  $\text{Sr}^{2+}$  ions resulted in increased proliferation and viability of MC3T3 cells cultured directly on the cement samples. Despite possessing low compressive strengths, all of the prepared cements remained structurally stable when immersed in both PBS and subsequently in the growth media for extended periods of time. Therefore, we believe the ACP/SrDCPD based cements could prove feasible as biodegradable non-load bearing scaffolds.

Future studies are however, needed to be conducted to further understand the cement system include evaluation of the Sr/(Ca+P) ratio in the cements during immersion in PBS. By knowing the exact Sr/(Ca+P) ratio at different time points during the phase transformation to SrHAp, we can better understand the level of Sr substitution within the HAp lattice. Another study

that needs to be performed is in-vitro assessment of osteoclasts cultured directly on the SrHAP scaffolds. As discussed in the prior work, Sr ions enhance proliferation and differentiation of osteoblasts as well as inhibit osteoclasts. Therefore, it would be beneficial to evaluate and verify the exact role of  $\text{Sr}^{2+}$  ions released from the SrHAP cements on the osteoblasts and osteoclasts in-vitro.

In order to make the SrHAP cements more attractive clinically, the setting time of the cements needs to be adjusted closer to the desired clinical setting time. In order to achieve faster setting times a reduction of the precursor particle sizes need to be realized, especially DCPD, by a method such as high-energy mechanical milling. Additionally, an adjustment of the ACP:DCPD ratios can also be utilized to reduce the setting time. By decreasing the amount of highly reactive ACP within the system, less of the liquid phase would be required, and thus resulting in decreased setting times. Another approach would be to modify the synthesis of the ACP phase by incorporation of other divalent ions that will help stabilize the amorphous phase in a much more reproducible fashion replicating the particle sizes and the amorphous disorder thereby exhibiting consistent solubility and stability in-vitro.

In order to improve corrosion resistance of UHD LAZ and LZ alloys, surface treatment via MAO was used to create corrosion resistant ceramic oxide-based coatings. The MAO coatings on all of the alloys within this studied resulted in a significant increase in corrosion resistance as compared to the bare alloys. The results concluded that Li content played a negative role on the corrosion resistance and stability of the MAO coatings in HBSS, whereas Al enabled the formation of additional stable phases within the MAO coating resulting in increased corrosion resistance and stability. Despite the increased corrosion resistance of the MAO coated alloys, only MAO coated LAZ631 was capable of enabling attachment and proliferation of MC3T3 cells when seeded

directly onto the coating. In order to further investigate this observation, indirect cell studies should be performed to assess only the dissolved ions effect on cytocompatibility. Future work for the biodegradable bioceramic MAO coatings should be aimed at increasing the compatibility of the coatings. Such methods could include the deposition of a secondary bioactive CaP coating that could assist in corrosion resistance by filling the pores on the surface of the MAO coatings. Finally, the true biological efficacy of both systems would only be realized by conducting in-vivo studies in relevant animal models such as rabbit and rat in subcutaneous, muscle ectopic as well as bone defect models. These studies will help ascertain the true safety, osteogenic differentiation and bone forming efficacy of the two systems studies herein.

## Bibliography

- [1] S. De, U.S. Orthopedic Devies Market to Witness Massive Growth Over 2017-2024, (2018).
- [2] F. Barrère, T.A. Mahmood, K. de Groot, C.A. van Blitterswijk, Advanced biomaterials for skeletal tissue regeneration: Instructive and smart functions, *Materials Science and Engineering: R: Reports* 59(1-6) (2008) 38-71.
- [3] X. Yu, X. Tang, S.V. Gohil, C.T. Laurencin, Biomaterials for Bone Regenerative Engineering, *Adv Healthc Mater* 4(9) (2015) 1268-85.
- [4] Z. Sheikh, S. Najeeb, Z. Khurshid, V. Verma, H. Rashid, M. Glogauer, Biodegradable Materials for Bone Repair and Tissue Engineering Applications, *Materials (Basel)* 8(9) (2015) 5744-5794.
- [5] M.R. Allen, D.B. Burr, Chapter 4 - Bone Modeling and Remodeling, in: D.B. Burr, M.R. Allen (Eds.), *Basic and Applied Bone Biology*, Academic Press, San Diego, 2014, pp. 75-90.
- [6] J. Hollinger, Bone Dynamics, in: J. Lieberman, G. Friedlaender (Eds.), *Bone Regeneration and Repair*, Humana Press 2005, pp. 1-19.
- [7] J.R. Perez, D. Kouroupis, D.J. Li, T.M. Best, L. Kaplan, D. Correa, Tissue Engineering and Cell-Based Therapies for Fractures and Bone Defects, *Front Bioeng Biotechnol* 6 (2018) 105.
- [8] P. Jayakumar, L. Di Silvio, Osteoblasts in bone tissue engineering, *Proceedings of the Institution of Mechanical Engineers, Part H: Journal of Engineering in Medicine* 224(12) (2010) 1415-1440.
- [9] P. Jayakumar, L. Di Silvio, Osteoblasts in bone tissue engineering, *Proc Inst Mech Eng H* 224(12) (2010) 1415-40.
- [10] C. Steffi, Z. Shi, C.H. Kong, W. Wang, Modulation of Osteoclast Interactions with Orthopaedic Biomaterials, *J Funct Biomater* 9(1) (2018).
- [11] R.P. Pirraco, A.P. Marques, R.L. Reis, Cell interactions in bone tissue engineering, *J Cell Mol Med* 14(1-2) (2010) 93-102.
- [12] H. Qu, H. Fu, Z. Han, Y. Sun, Biomaterials for bone tissue engineering scaffolds: a review, *RSC Advances* 9(45) (2019) 26252-26262.
- [13] P. Chakraborty Banerjee, S. Al-Saadi, L. Choudhary, S.E. Harandi, R. Singh, Magnesium Implants: Prospects and Challenges, *Materials (Basel)* 12(1) (2019).

- [14] C. Liu, Z. Ren, Y. Xu, S. Pang, X. Zhao, Y. Zhao, Biodegradable Magnesium Alloys Developed as Bone Repair Materials: A Review, *Scanning* 2018 (2018) 9216314.
- [15] M. Valletregi, Calcium phosphates as substitution of bone tissues, *Progress in Solid State Chemistry* 32(1-2) (2004) 1-31.
- [16] S. Dorozhkin, Calcium Orthophosphate Cements and Concretes, *Materials* 2(1) (2009) 221-291.
- [17] Z. Tao, W. Zhou, Y. Jiang, X. Wu, Z. Xu, M. Yang, J. Xie, Effects of strontium-modified calcium phosphate cement combined with bone morphogenetic protein-2 on osteoporotic bone defects healing in rats, *J Biomater Appl* 33(1) (2018) 3-10.
- [18] M. Schumacher, M. Gelinsky, Strontium modified calcium phosphate cements – approaches towards targeted stimulation of bone turnover, *Journal of Materials Chemistry B* 3(23) (2015) 4626-4640.
- [19] E. Boanini, M. Gazzano, A. Bigi, Ionic substitutions in calcium phosphates synthesized at low temperature, *Acta Biomater* 6(6) (2010) 1882-94.
- [20] X. Wang, J. Ye, Y. Wang, Influence of a novel radiopacifier on the properties of an injectable calcium phosphate cement, *Acta Biomater* 3(5) (2007) 757-63.
- [21] G.M. Kuang, W.P. Yau, J. Wu, K.W. Yeung, H. Pan, W.M. Lam, W.W. Lu, K.Y. Chiu, Strontium exerts dual effects on calcium phosphate cement: Accelerating the degradation and enhancing the osteoconductivity both in vitro and in vivo, *J Biomed Mater Res A* 103(5) (2015) 1613-21.
- [22] Z. Li, X. Gu, S. Lou, Y. Zheng, The development of binary Mg-Ca alloys for use as biodegradable materials within bone, *Biomaterials* 29(10) (2008) 1329-44.
- [23] B.V. Vladimirov, B.L. Krit, V.B. Lyudin, N.V. Morozova, A.D. Rossiiskaya, I.V. Suminov, A.V. Epel'feld, Microarc oxidation of magnesium alloys: A review, *Surface Engineering and Applied Electrochemistry* 50(3) (2014) 195-232.
- [24] N. Nassif, I. Ghayad, Corrosion Protection and Surface Treatment of Magnesium Alloys Used for Orthopedic Applications, *Advances in Materials Science and Engineering* 2013 (2013) 1-10.
- [25] Y. Feng, X. Ma, L. Chang, S. Zhu, S. Guan, Characterization and cytocompatibility of polydopamine on MAO-HA coating supported on Mg-Zn-Ca alloy, *Surface and Interface Analysis* 49(11) (2017) 1115-1123.
- [26] G. Barati Darband, M. Aliofkhazraei, P. Hamghalam, N. Valizade, Plasma electrolytic oxidation of magnesium and its alloys: Mechanism, properties and applications, *Journal of Magnesium and Alloys* 5(1) (2017) 74-132.



- [27] W. J, Thesis, University of Pittsburgh (2018).
- [28] S. Singh, FUNDAMENTAL STUDY OF CATIONIC DOPED CALCIUM PHOSPHATE BASED SCAFFOLDS AND COATINGS FOR BONE TISSUE ENGINEERING, University of Pittsburgh (2015).
- [29] S.S. Singh, A. Roy, B.E. Lee, J. Ohodnicki, A. Loghmanian, I. Banerjee, P.N. Kumta, A study of strontium doped calcium phosphate coatings on AZ31, Mater Sci Eng C Mater Biol Appl 40 (2014) 357-65.
- [30] A. Roy, S.S. Singh, M.K. Datta, B. Lee, J. Ohodnicki, P.N. Kumta, Novel sol–gel derived calcium phosphate coatings on Mg4Y alloy, Materials Science and Engineering: B 176(20) (2011) 1679-1689.
- [31] J. Dou, Y. Chen, H. Yu, C. Chen, Research status of magnesium alloys by micro-arc oxidation: a review, Surface Engineering 33(10) (2017) 731-738.
- [32] L. Song, Y. Kou, Y. Song, D. Shan, G. Zhu, E.H. Han, Fabrication and characterization of micro-arc oxidation (MAO) coatings on Mg-Li alloy in alkaline polyphosphate electrolytes without and with the addition of K<sub>2</sub>TiF<sub>6</sub>, Materials and Corrosion 62(12) (2011) 1124-1132.
- [33] P. Tian, F. Peng, D. Wang, X. Liu, Corrosion behavior and cytocompatibility of fluoride-incorporated plasma electrolytic oxidation coating on biodegradable AZ31 alloy, Regen Biomater 4(1) (2017) 1-10.
- [34] X. Tu, C. Miao, Y. Zhang, Y. Xu, J. Li, Plasma Electrolytic Oxidation of Magnesium Alloy AZ31B in Electrolyte Containing Al(2)O(3) Sol as Additives, Materials (Basel) 11(9) (2018).
- [35] H.F. Guo, M.Z. An, H.B. Huo, S. Xu, L.J. Wu, Microstructure characteristic of ceramic coatings fabricated on magnesium alloys by micro-arc oxidation in alkaline silicate solutions, Applied Surface Science 252(22) (2006) 7911-7916.
- [36] F. Peng, D. Wang, Y. Tian, H. Cao, Y. Qiao, X. Liu, Sealing the Pores of PEO Coating with Mg-Al Layered Double Hydroxide: Enhanced Corrosion Resistance, Cytocompatibility and Drug Delivery Ability, Sci Rep 7(1) (2017) 8167.
- [37] M. Guo, L. Cao, P. Lu, Y. Liu, X. Xu, Anticorrosion and cytocompatibility behavior of MAO/PLLA modified magnesium alloy WE42, J Mater Sci Mater Med 22(7) (2011) 1735-40.
- [38] Y.K. Pan, C.Z. Chen, D.G. Wang, X. Yu, Microstructure and biological properties of micro-arc oxidation coatings on ZK60 magnesium alloy, J Biomed Mater Res B Appl Biomater 100(6) (2012) 1574-86.
- [39] K. Rokosz, T. Hryniewicz, S. Gaiaschi, P. Chapon, S. Raaen, W. Malorny, D. Matysek, K. Pietrzak, Development of Porous Coatings Enriched with Magnesium and Zinc Obtained by DC Plasma Electrolytic Oxidation, Micromachines (Basel) 9(7) (2018).

- [40] H.H. Xu, P. Wang, L. Wang, C. Bao, Q. Chen, M.D. Weir, L.C. Chow, L. Zhao, X. Zhou, M.A. Reynolds, Calcium phosphate cements for bone engineering and their biological properties, *Bone Res* 5 (2017) 17056.
- [41] N.M. Van den Vreken, I.Y. Pieters, H.A. Declercq, M.J. Cornelissen, R.M. Verbeeck, Characterization of calcium phosphate cements modified by addition of amorphous calcium phosphate, *Acta Biomater* 6(2) (2010) 617-25.
- [42] T. Yu, J. Ye, Y. Wang, Preparation and characterization of a novel strontium-containing calcium phosphate cement with the two-step hydration process, *Acta Biomater* 5(7) (2009) 2717-27.
- [43] C. Combes, C. Rey, Amorphous calcium phosphates: synthesis, properties and uses in biomaterials, *Acta Biomater* 6(9) (2010) 3362-78.
- [44] M.G. D. Knaack, M. Aiolo, C. Rey, A. Tofighi, P. Chakravarthy, et al., Resorbable calcium phosphate bone substitute, *J Biomed Mater Res (Appl Biomater)* 43 (1998) 11.
- [45] A.T. DD. Lee, P. Chakravarthy, A. Majahad, et al., alpha-BSM: a biomimetic bone substitute and drug delivery vehicle, *Clin Orthop Relat Res* 367s (1999) 10.
- [46] P. Habibovic, J.E. Barralet, Bioinorganics and biomaterials: bone repair, *Acta Biomater* 7(8) (2011) 3013-26.
- [47] S.S. Singh, A. Roy, B. Lee, S. Parekh, P.N. Kumta, Murine osteoblastic and osteoclastic differentiation on strontium releasing hydroxyapatite forming cements, *Mater Sci Eng C Mater Biol Appl* 63 (2016) 429-38.
- [48] Y. Li, T. Wiliana, K.C. Tam, Synthesis of amorphous calcium phosphate using various types of cyclodextrins, *Materials Research Bulletin* 42(5) (2007) 820-827.
- [49] D. Lee, C. Sfeir, P.N. Kumta, Novel in-situ synthesis and characterization of nanostructured magnesium substituted  $\beta$ -tricalcium phosphate ( $\beta$ -TCMP), *Materials Science and Engineering: C* 29(1) (2009) 69-77.
- [50] A. Tofighi, A. Rosenberg, M. Sutaria, S. Balata, J. Chang, New Generation of Synthetic, Bioresorbable and Injectable Calcium Phosphate Bone Substitute Materials: Alpha- $\beta$ -BSM<sup>®</sup>, Beta-BSM<sup>TM</sup> and Gamma-BSM<sup>TM</sup>, *Journal of Biomimetics, Biomaterials and Tissue Engineering* 2 (2009) 39-55.
- [51] R.-C. Zeng, W.-C. Qi, Y.-W. Song, Q.-K. He, H.-Z. Cui, E.-H. Han, In vitro degradation of MAO/PLA coating on Mg-1.21Li-1.12Ca-1.0Y alloy, *Frontiers of Materials Science* 8(4) (2014) 343-353.

[52] Y.K. Liu, Q.Z. Lu, R. Pei, H.J. Ji, G.S. Zhou, X.L. Zhao, R.K. Tang, M. Zhang, The effect of extracellular calcium and inorganic phosphate on the growth and osteogenic differentiation of mesenchymal stem cells in vitro: implication for bone tissue engineering, *Biomed Mater* 4(2) (2009) 025004.